SiGe Electro-Absorption Modulators for Applications at 1550nm

by
Sarah Bernardis

Laurea in Physics
Università degli Studi di Padova, 2005

Submitted to the Department of Material Science and Engineering in Partial Fulfillment of the Requirements for the degree of

Master of Science in Materials Science and Engineering
at the
Massachusetts Institute of Technology

February 2008

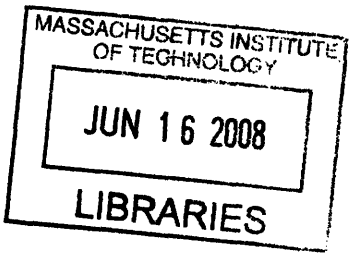

Signature of Author:_____
Department of Materials Science and Engineering
January 22, 2008

Certified by:_____
Lionel C. Kimerling
Thomas Lord Professor of Materials Science and Engineering
Thesis Supervisor

Certified by:_____
Jurgen Michel
Department of Materials Science and Engineering
Thesis Supervisor

Accepted by:_____
Samuel M. Allen
POSCO Professor of Physical Metallurgy
Chair, Departmental Committee on Graduate Students

SiGe Electro-Absorption Modulators for Applications at 1550nm
by
Sarah Bernardis

Abstract

A novel Si_xGe_{1-x} electro-absorption modulator design is experimentally demonstrated. The device is waveguide integrated, butt-coupled into high index contrast Si/SiO_2 waveguides. 0.75% Silicon concentration in the alloy is optimized for 1550nm applications. With its 400nm height, 600nm width, and 50μm length, the device has a footprint smaller than 30μm^2. Low effective driving voltage, <2.5V, is needed to achieve an extinction ratio of 5.2dB in the broad 1510-1555nm wavelength operation range. At 1550nm, an extinction ratio of 6.5dB is achieved with an applied effective bias of -2.5V.

High frequency measurements determine the device can reach a 3dB frequency of 1.2GHz. Electrical characterization of the device shows high series resistance ($\sim$15kΩ) which is caused by fabrication over-etching during metal contact deposition. Series resistance reduction to $\sim$100Ω would allow the device to reach the predicted 3dB frequency of 100GHz with 10dB extinction ratio.

A pseudo-linear relation is found between the achieved extinction ratio and the applied effective bias. The ratio between these two quantities, the modulation efficiency, can be considered as a new figure of merit of the device. The slope of this pseudo-linear relation measures 2.2dB/V for extinction ratio values ranging between 0 and 5.5dB. In terms of modulation depth it is equivalent to a slope of 40%/V in the range 0.5V-2V. Finally, an ultra-low power consumption per bit of 34fJ/bit is measured for a capacitance of 11fF and an effective applied reverse bias of 2.5V.

Thesis Supervisor: L.C. Kimerling
Title: Thomas Lord Professor of Materials Science and Engineering

Thesis Supervisor: J. Michel
Title: Department of Materials Science and Engineering

Acknowledgments

This thesis is like a hand blown glass pumpkin.

Blowing a glass pumpkin requires a starter, a gaffer, and a stemmer. The starter, the most challenging task among the three, gathers the glass, colors it, and molds it. The gaffer puts the neckline in and decides the final shape while the stemmer blows and, as the name suggests, makes the stem. The stemmer has the task of finishing a pumpkin that encloses the personality of three people. Three people that worked together to create a unique piece.

In this regard this thesis is like a hand blown glass pumpkin. To my starters, Prof. L.C. Kimerling and Dr. J. Michel, starters of this project, always full of ideas and motivation. The gaffer, Dr. J. Liu, sharing his modulator design and more importantly insites on what/ how/ why/ and more. I would like to thank you all for giving me the chance of being your stemmer.

Finally, a special "thank you" to J. Cheng, for all the help with the high speed measurement set-up.

Contents

List of Figures

List of Tables

Chapter 1

Introduction

The aim of this thesis is to provide a comprehensive understanding of the importance of modulators in electronic-photonic integration. The figure of merit of desirable modulators is characterized by small footprint size, low driving voltage, and high modulation depth and speed. It is absolutely challenging to fulfill simultaneously all the above criteria with the additional requirements of low insertion loss and temperature independent performance. This thesis presents a unique design of waveguide integrated modulators with small footprints, low driving voltages, and a large operational bandwidth over the entire C-band wavelength range.

1.1 Motivation

Telecommunication and on-chip interconnects are about to reach a bottleneck. As fabrication nodes decrease feature size capabilities, transistors can be shrunk down more, but metal interconnects do not keep up quite as well with the shrinking process. Two major problems arise as miniaturization oc-

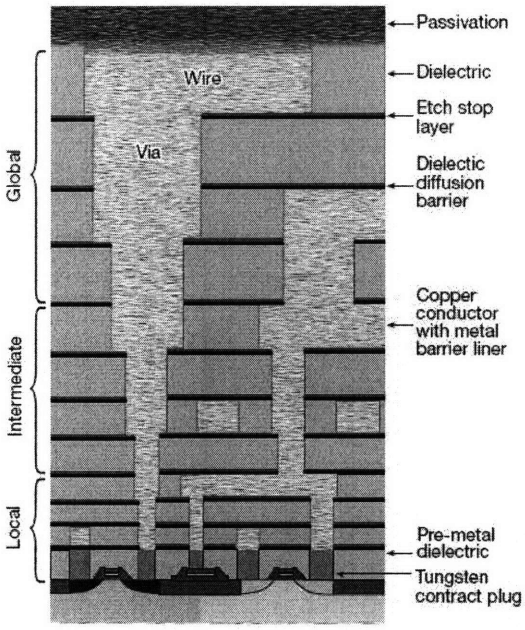

Figure 1.1: Example of a 10-layer metal interconnect: projected structure for the 35nm technology node [1]. Interconnect levels are divided in local, intermediate, and global.

curs. Below the 150nm node, interconnect RC delay increases as feature size decreases causing signal desynchronization in clock distribution, resulting in higher bit error rates. Secondly, heat dissipation due to the on-chip length of these interconnects causes major problems. Thus, metal interconnects are far from being ideal for high speed data transmission and are a clear bottleneck to potential performance improvements of new microprocessors. An example of metal interconnect is in Figure 1.1.

A viable way of overcoming this challenge would be the integration of photonics with microelectronics. Data would need to be collected, routed, modulated, detected in a very small space and in a very efficient way. Optical interconnects (Figure 1.2) would have the advantage of low power requirements, low latencies, high bandwidth and no heat dissipation issues, since photons do not generate heat as they propagate through waveguides. On-

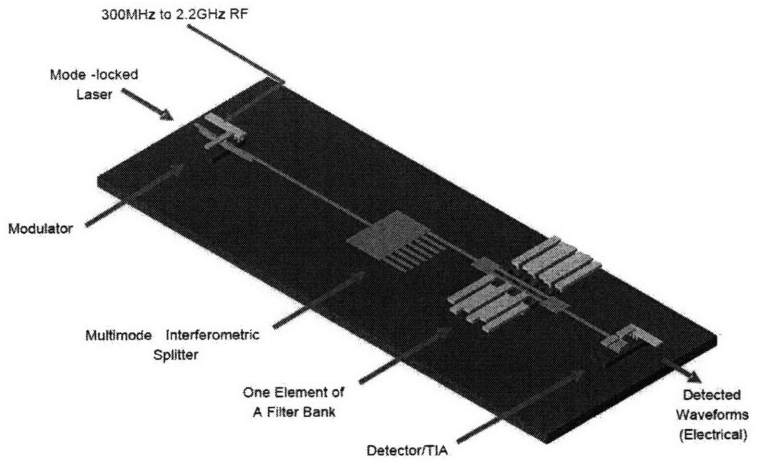

Figure 1.2: Example of an optical link. Light source (on- or off-chip), modulator, detector, and waveguides are the most important components of such a link.

chip communication between standard CMOS electronic components and photonic devices would mainly be carried out by a light source, modulator, detector, and waveguides to connect these three devices. Mainly, the modulator would imprint 0s and 1s on the on-chip or off-chip generated light signals and the photodetector would convert these signals back to electrical ones.

Integration of Silicon photonic interconnects with microelectronics would represent a revolutionary breakthrough for the next generation of communication tools as well as computing platforms. Among optical devices, modulators are the ones with highest power consumption. Therefore, they represent the most critical component for enabling this integration to happen. The focus of this thesis is a SiGe electro-absorption modulator design with small

footprint and low driving voltage, hence ensuring low power consumption.

Integration of electronics and photonic devices would be greatly enhanced if the same facilities and technology could be used. Silicon is the main material used for electronics but it poses some challenges for photonic components such as high propagation losses, low electrooptic coefficient, high fiber-to-waveguide coupling losses. Nanofabrication improvements are slowly solving each one of these problems. Nowadays, ultra-compact micrometer size, high-performance active and passive photonic components are being demonstrated. Thus, Silicon optical interconnects would allow CMOS monolithic integration and ultra-fast signal processing, allowing for novel chip architectures to be exploited.

Drawback of Silicon is that its direct band gaps are in the range 3-4eV. An alternative material is Germanium which is also CMOS compatible and its direct band gap is 0.8eV, corresponding exactly to the wavelength of 1550nm. For wavelengths just smaller than 1550nm, Germanium has good quantum efficiency in photon absorption. Electron mobility (3900 $cm^2/s{\cdot}V$) and hole mobility (1900 $cm^2/s{\cdot}V$) are both better than in elemental Silicon. It is expected that Germanium devices will be faster and will operate with lower bias with respect to the same Silicon devices.

Being both elemental materials CMOS compatible, their alloy, SiGe is also CMOS compatible. The optoelectronic properties of this alloy are promising for modulating applications. Especially, its electro-absorption properties are of current research interest.

SiGe electro-absorption modulators integrated in high index contrast waveg-

uides are investigated in this thesis. These devices are based on the Franz-Keldysh effect where an applied electric field enhances the absorption coefficient in the weakly absorbing regime. Device design is optimized for 1550nm operations.

This thesis will explain why SiGe is used, how to design the electro-absorption modulator and how it physically works, and finally how to measure it once it is fabricated. As background knowledge, this first introductory chapter will summarize published results of other research groups, why their ideas are great, what it is possible to learn from them, especially how their designs work. The second chapter will explain the physical principles behind the working device; it will consider material's characteristics that will be exploited in the device design, the device design itself, its optimization, and briefly its fabrication. The third chapter will prove experimentally how incredibly well this SiGe electro-absorption modulator performs. Finally, the fourth chapter will summarize key points and look into the future.

1.2 Modulators: General Overview

As G Parry wrote in a brief column in Nature, *A modulator is analogous to a camera shutter: it transmits light when it is open, but absorbs light when it is closed*, [2]. This section is meant to explore this picture of the shutter mechanism, considering which parameters are of fundamental importance when evaluating its performance for applications at 1550nm. Physical mechanisms leading to modulation will be considered in the next section.

Several different types of modulators have been demonstrated. The physics used to achieve modulation as well as the design of the structure highly influence the performance of the device. In order to understand which devices work best, a few key common parameters can be compared. These parameters are: device footprint, driving voltage (both dc and ac bias), modulation depth, switching speed (also rise and fall times), bandwidth, insertion loss, wavelength sensitivity, and temperature sensitivity.

On-chip optical interconnects need to fit with the always shrinking electronic counterpart: device footprint needs to be small, possibly reaching the physically limited dimensions of the wavelength of light being used. As these devices are monolithically integrated, the driving voltage has limitations imposed by the node at which they are fabricated. As an example, at the 90nm node, only a voltage smaller than 1V will be allowed. In turn, the applied voltage determines the achievable modulation depth. The modulation depth is one of the key parameters of the device. It is measured in decibels and it represents the optical output intensity ratio between the "off" and "on" states of the modulator. If this ratio is large, the intensity output difference between the "on" and "off" states of operation is large and the signal-to-noise ratio is consequently also high. Devices reported in the literature generally only fulfill a few of these requirements.

In Mach-Zehnder devices, the applied voltage required to achieve a π-radian phase shift also depends on the length of the arm of the interferometer. The product of these two quantities, voltage and arm length, is usually considered figure of merit of the device, $V_\pi \cdot L_\pi$. Goal is to minimize this

product.

Device fabrication tolerance represents a challenge when an operational wavelength is predefined: wavelength sensitivity is one of the major concerns in devices such as ring modulators. Moreover, temperature sensitive devices, such as ring resonators, can easily get detuned as a bias is applied. As carriers flow, the temperature increases and the optical properties change. Even small temperature changes can drastically compromise device performance.

Another fundamental parameter is the available bandwidth of operation. It represents the amount of data that can be carried and modulated in a unit time. It is calculated to be the difference between the upper and lower frequencies at which the modulation depth falls to 50% of its maximum value.

Gathering these concepts together into a quantitative expression, a general figure of merit, independent of device design, could be given by the ratio:

$$\text{Figure of Merit} = \text{Bandwidth} \;/\; \text{Power} \cdot \text{Device Footprint}$$

In the case of an electro-absorption modulator, a simple figure of merit is the ratio between the modulation depth ($\Delta\alpha$) and the insertion loss at the optical "on" state (α_{on}):

$$\text{Electro-absorption Modulator} = \frac{\Delta\alpha}{\alpha_{on}},$$

since the former should be as high as possible and the latter, instead, as low as possible. On the optical "on" state, the modulator is supposed to be completely transparent to light. Insertion loss refers to optical power loss due

to material absorption, sidewall scattering due to surface roughness, and loss due to optical mode mismatch between the waveguide and the modulator structure. High insertion losses deteriorate the optical output. Insertion loss and modulation depth are mathematically defined as:

$$\text{Insertion Loss} = -10\log\{e^{-\alpha_{on}\cdot L}\}$$
$$\text{Modulation Depth} = -10\log\left\{\frac{e^{-\alpha_{off}\cdot L}}{e^{-\alpha_{on}\cdot L}}\right\}$$

where α_{on} refers to the absorption coefficient at the optical "on" state, α_{off} to the optical "off" state, and L is the device length.

1.3 Modulator Physical Principles

Light modulation in Silicon based devices implies a change in the optical field due to some applied signal. This signal is typically electrical, but other parametric changes are possible. These parametric changes modify the refractive index seen by the propagating optical mode. Using an electrical signal, the most efficient way of implementing optical modulation in Silicon is through carrier injection or depletion.

Free carriers can be injected either optically with a pump laser or electronically with a p-i-n diode (usually under forward bias). Other CMOS devices, such as metal-oxide-semiconductor (MOS), have been used especially in carrier inversion mode. Devices that work at a few GHz have been demonstrated both with Mach-Zehnder and ring resonator structures. Drawback of carrier injection is that the recombination time is of the order of nanoseconds, thus limiting the device speed. A reverse bias could be applied to sweep out the

carriers faster, but their transit time would still be a limiting factor. Also, carrier injection happens only under high current, leading to higher power consumption. In the case of rings, also, there is a tradeoff between high quality factor and speed. The higher the quality factor, the higher the photon lifetime in the cavity, and the higher the delay in modulation. The lower the quality factor, the lower the modulation depth (i.e. the contrast between resonant and non-resonant wavelength becomes smaller).

In the following remaining of this section, mechanisms exploited to modulate Silicon based devices at 1550nm are briefly explained.

1.3.1 Electro-optic Effect

A change in the real part of the refractive index with an externally applied electric field is called *electro-refraction*, while a change in the imaginary part of the refractive index is called *electro-absorption*.

Electro-refraction Effects Even though other integrated optical technologies exploit electro-refraction, it is not useful in Silicon. The two main electro-refraction effects are Pockels and Kerr effects. The Pockels effect, a change in refractive index linearly proportional to the applied electric field, is polarization dependent and it is not present in Silicon due to its crystallographic structure. The Kerr effect, a second-order electric field effect, is present in Silicon but it is extremely weak. Besides, this effect is extremely small compared to carrier injection effects.

Electro-absorption Effect This effect is known as Quantum Confined Stark Effect in quantum well devices and as Franz-Keldysh Effect in bulk material. The refractive index is rapidly modified by field effects. In the case of the Franz-Keldysh effect, it induces a change in both the real and imaginary parts of the refractive index. When reverse biasing a p-i-n junction, a high electric field is generated in the intrinsic layer. This field induces changes in both real and imaginary parts of the refractive index. However, the electro-absorption effect is stronger of the two. It distorts the energy bands of the semiconductor, shifting the band gap energy, which in turn modifies the absorption properties of the material (i.e. the imaginary part of the refractive index), particularly at wavelengths close to the band gap.

As the electric field is turned "on" and "off", the material becomes transparent or opaque to specific wavelengths. Devices that rely on this effect can theoretically reach modulating speeds of tens of GHz as the response of the material to the electric field happens in the picosecond time range. The reverse bias applied to the junction allows for smaller current to flow in the device with respect to devices that work under forward bias, as the ones that exploit free carrier injection: device comparison shows lower power required to achieve the same modulation depth.

1.3.2 Carrier Injection and Depletion

Optical losses are enhanced by material absorption which is due to the presence of free carriers. The imaginary part of the refractive index is related to the loss coefficient. Hence, modification of the carrier concentration im-

plies a change in the refractive index. Free carrier injection decreases the refractive index inducing intensity modulation. Injection, depletion, accumulation, and inversion are all mechanisms that modify the free carrier concentration in carrier dispersion devices. Electrical structures such as p-i-n diodes, metal-oxide-semiconductors field-effect transistors, and bipolar-mode field-effect transistors allow this mechanism to be exploited.

1.3.3 Thermo-optic Effect

If the real part of the refractive index is temperature dependent, phase modulation of the transmitted light can be induced by local variation of the temperature. Also, while the thermo-optic effect induces a red shift (i.e. it increases the refractive index), the carrier injection or depletion effect causes a blue shift (i.e. the refractive index decrease). Interference of the two mechanisms should be considered during device design and operation. Drawback of this mechanism is slow frequency modulation (MHz). For this reason, devices relying only on this effect will not be considered in the following.

1.3.4 All Optical Mechanism

All optical modulation relies on optical retardation. One beam of light (pump beam) is used to control a second beam of light (probe beam). An index change is produced and it induces a phase shift in the propagating wave. This phase shift is converted to an intensity shift through the structure of the device (i.e. using an interferometric structure). There are two ways of achieving all optical modulation: either by thermo-optic non-linear effect

	All-Optical Modulation		Bias Induced Modulation	
	All-Optical	Optical Bistability	p-i-n	MOS
Ring Resonator	[6]-[8]	[9], [10]	[11]-[16]	[17], [18]
Mach-Zehnder	[19]		[20]-[22]	[23]-[27]
Fabry-Pérot	[28]		[29]-[31]	

Table 1.1: Selected published results on Silicon based modulators operating at 1550nm presented in this chapter. Optical structure versus bias design.

induced by the large Silicon thermo-optic coefficient; or by carrier induced effects. These two effects in conjunction with device structure (Mach-Zehnder and ring resonator) are described in the following section.

All optical modulation enables for ultra-fast signal processing, overcoming the optics-to-electronics conversion limitation.

1.4 Modulator Optical Structure Design

While examining the principles of operation of all different combinations of optical and electrical structures as of now demonstrated, recently published results (2004-2007) will be explained to provide a hands-on feeling of what these structures are capable of. A variety of different structures for applications at 1550nm have been simulated and sometimes also fabricated and tested as schematized in Table 1.1.

The three main optical structures are ring resonators, and Mach-Zehnder or Fabry-Pérot interferometers. There can be no bias involved as in the case of all optical modulation, or these devices can have p-i-n embedded

structures, or MOS configuration. Different matching of optical structure and electrical structure allows for different achievable performance.

1.4.1 Ring Resonators

Before listing different ring configurations that are found in the literature, a few key concepts that are common to the geometrical structure itself are here summarized. Reference papers on this topic are [3]-[5].

Rings are wavelength selective resonant structures. Light is evanescently coupled from an adjacent waveguide to the ring cavity. The ring circumference determines the resonant wavelength: only light with wavelength equal to an integer multiple of the ring circumference will be trapped reducing transmission at the through waveguide port. The amount of light evanescently coupled from the waveguide to the ring is of fundamental importance and it depends on the gap between the two structures. Another very important parameter is the lifetime of photons in the resonator. As a general rule of thumb, a high cavity quality factor implies strong light confinement and hence strong wavelength dependence on the index of refraction of the ring, which in turn implies high modulation. High switching speed is, on the other hand, achieved with low photon lifetime, i.e. low quality factor. High transmittance is detected when there is low total insertion loss.

A ring is a multi-pass device: at resonance, light travels multiple times inside the device in round trips, increasing the optical path length and leaving the physical device length unmodified. Less carriers are needed to achieve the targeted modulation depth because light has multiple interactions with them:

less power is required to drive carriers in and out of the device. Also, ring resonators are optimized to modulate light of a specific wavelength. Light of all other wavelengths is not affected by the ring structure. This makes ring resonators extremely interesting for wavelength division multiplexing applications. Drawback of the ring resonator is that it is highly temperature sensitive. Oxidation induced strain between the Silicon core and oxide cladding is suggested to diminish temperature variation issues, [10].

Typically, rings are either used for all optical modulation or they are externally biased to obtain free carrier effects. All optical modulation exploits non-linear optic effects in two main ways: the first one uses two beams of light, the first beam changes the optical properties of the material, while the second one is being modulated; the second method involves optical bistability effects induced by one- or two-photon absorption mechanisms. Both methods are experimentally demonstrated ([9] and [10]).

All Optical Modulation All optical modulation relies on two beams of light: the first one controls the properties of the waveguide material, which, in turn, directly affect the second one. A control beam and probe beam are coupled into the ring through two different resonances. The control beam generates free carriers by (one- or) two-photon absorption effect, triggering the plasma dispersion effect which reduces the refractive index of the ring waveguide. A small change in refractive index is sufficient to detune the resonance of the probe beam. In fact the probe resonance experiences a blue-shift which induces modulation of its output power. As the control beam is

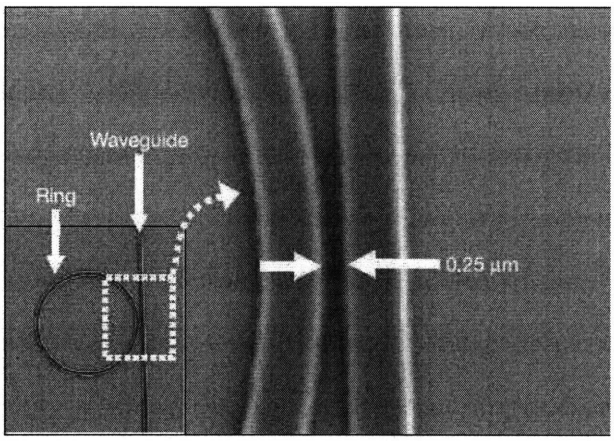

Figure 1.3: SEM picture of a 10μm diameter ring modulator coupled to a waveguide, [6]

switched off, the probe resonance shifts to its original position thanks to the free carrier recombination.

Almeida [6] (and Lipson [7]) exploits all optical modulation due to two-photon absorption in a ring with 10μm diameter (Figure 1.3). The probe wavelength used is 1535nm while the pump wavelength is 1550nm with 10ps pulse duration. Probe and pump cavity photon lifetime are 1.8ns and 2.8ps, respectively. Just below resonance, at 1535nm, the measured modulation depth is 94% (12.2dB); on resonance, 1535nm, 91% (10.45dB); and above resonance (1554nm and 1550nm), 75% and 97%. The relaxation time is 450ps and it is determined by the recombination of photoexcited free carriers on the unpassivated sidewalls of the structure.

Two-photon absorption is used also in another ring device by Xu [8]. It is optimized for high speed measurements as wavelength conversion rather than modulation. "On" resonance, light is trapped inside the ring and light that is back-coupled to the through waveguide is destructively interfering with directly transmitted light. When the resonator shifts from "on" resonance

to "off" resonance, little coupling between the input waveguide and the ring resonator happens: light mainly propagates through the waveguide; only the small amount of light that couples to the ring experiences a temporal refractive index change in the ring which in turn generates a wavelength shift. As this wavelength-shifted light back-couples to the through waveguide, no destructive interference is measured. Instead, overshoots and damped oscillations due to beating effects are noticed. The former is determined by the cavity photon lifetime, while the wavelength shift determines the frequency of the latter. The ring has 10μm diameter, resonance wavelength is 1550nm, cavity photon lifetime is 9.1ps; wavelength conversion happens with a speed of 0.9Gbit/s. Implementing the structure with a p-i-n junction, the expected carrier lifetime is 30ps with a wavelength conversion rate of 10Gbit/s.

Manolatou [5] simulates two-photon absorption in two rings of 2 and 5μm radiuses. Resonant wavelengths are 1561 and 1558nm, respectively. Modulation depth of ~90% can theoretically be achieved with both rings: in the case of the 2μm one, the pump energy is 1.25pJ, where the required energy to generate the free carrier concentration is 0.042pJ; while in the case of the 5μm ring, the pump energy is 3pJ and the energy required to generate the needed free carrier concentration is only 0.1pJ.

Optical Bistability due to Thermo-optic Effect Measuring the transfer function of the ring (i.e. fixing the input wavelength and detecting the transmitted power versus input power), a resonance shift is seen due to

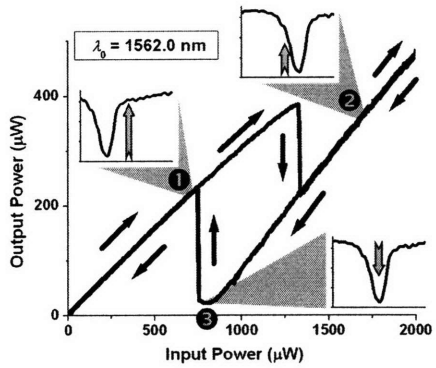

Fig. 3. Hysteresis curve for the quasi-TE mode of a SOI ring resonator excited at λ_0 = 1562.0 nm. Markers define curve points related to the transmission spectra in the insets: ❶ unshifted spectrum on the linear region before hysteresis loop, ❷ shifted spectrum due to high-input increasing power, ❸ resonance shifted to pump wavelength.

Figure 1.4: Modulation mechanism by thermo-optic induced optical bistability explained by Almeida, [9].

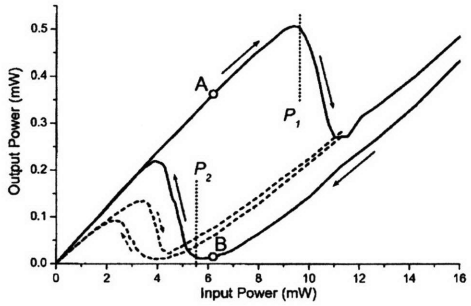

Figure 1.5: Modulation mechanism by carrier induced optical bistability, [10].

thermo-optic effects. Transmission is affected because the resonance shift depends on the optical power circulating in the ring. A hysteresis loop is created as this circulating optical power is determined by the wavelength difference between the optical source and the shifted resonance. Using a ring with a 10μm diameter and a 100kHz square modulated 1561nm pump wavelength Almeida [9] experimentally show that 8dB modulation can be achieved with 250μW of power required for switching. Instead, if constant optical power of 550μW is supplied through the pump wavelength, less than 45μW are required to achieve 10dB modulation on a probe wavelength of 1580nm.

Optical Bistability due to Carrier-Induced Effect Carrier-induced bistability relies on generation of free carriers by two-photon absorption. Free

carriers reduce the refractive index inducing a blue-shift in the ring resonator spectrum.

If the starting optical pulse has shorter wavelength than the resonant wavelength of the ring, free carrier concentration in the ring is low. However, the optical pulse will produce free carriers inducing resonance blue-shifting. The blue-shift itself will enhance free carrier generation causing more blue-shifting. This induces a positive feedback loop that feeds itself until the wavelength of the input optical pulse becomes longer than the resonant wavelength of the ring. The blue-shift process stabilizes when the induced blue-shift becomes large enough and the wavelength of the input optical pulse becomes longer than the ring resonant wavelength, the positive feedback becomes negative. A hysteresis loop is seen when this positive feedback loop becomes negative (Figure 1.5).

Carrier induced optical bistability is reported by Xu [10] at a wavelength of 1532nm in a ring with 10μm diameter and quality factor of 14,000. The effect is achieved with power smaller than 10mW. The reported transmission drop at resonance is of 14dB.

Thermo-optic and carrier induced bistability effects are compared in the same paper [10]. Experimental observations show that for the same input optical pulse width (23ns), thermo-optic induced bistability prevails on carrier induced bistability. Also, in order to obtain the same results using the two mechanisms separately, the required input optical power required to trigger the thermooptic mechanism is one order of magnitude smaller than that required to trigger carrier induced effects (10mW).

Externally Applied Bias When an externally applied bias is used to induce free carrier effects, two structures are widely used in the literature: p-i-n junctions and MOS structures [11].

p-i-n junctions are better to achieve high speed modulation. In terms of optical and electrical confinement, the optical mode traveling in the waveguide has greater overlap with the region where the index of refraction changes due to the applied bias (electrical region) [12]. Clear drawback is that if extraction of carriers under reverse bias happens in the picosecond range, carrier injection under forward bias happens in the nanosecond range. A decreased injection time can be achieved with a resonant p-i-n structure where the rise and fall times are enhanced.

p-i-n and p-i-n-i-p Configurations Free carriers are injected in the intrinsic region of the device through a p-i-n junction embedded in the ring structure. An electric field is generated where the waveguide lies. The refractive index is modified as well as the ring resonant wavelength. This produces signal modulation of the transmitted light. Carrier injection is obtained forward biasing the junction, while to sweep out electron-hole pairs faster and achieve higher modulation speed, the junction is reverse biased. High speed modulation can be achieved when optical transmission reaches its maximum before the electrical junction reaches steady-state and optical rise time is shorter than electrical rise time.

A milestone paper on ring performance is a Nature paper by Xu [12]. Their research team fabricated a 12μm diameter ring (Figure 1.6) with qual-

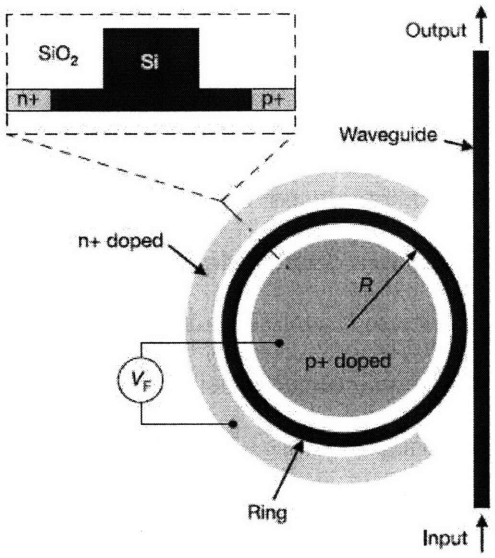

Figure 1.6: Top view of a ring modulator coupled to a waveguide. Inset shows the ring modulator cross-section with the embedded p-i-n junction [12].

ity factor of 39,350 and a cavity photon lifetime of 33ps. Static measurements show 15dB extinction ratio with a forward bias of 0.94V and reverse bias of -0.3V. Device speed is 0.4Gbit/s when a non-return to zero input signal is used and a peak to peak voltage (V_{pp}) of 3.3V_{pp} (-1.85V, +1.45V); if a return to zero signal is used, then the speed is 1.5Gbit/s with 6.9V_{pp} (-2.8V, +4.1V). In this latter case, 200ps rise time and 150ps fall time are measured.

Of the same research group, further experimental results are presented by Preble [13]. A ring of the same diameter (12μm) is used under reverse bias conditions to show that by using a pump wavelength of 1528nm and a probe wavelength of 1559nm, 6.8dB extinction ratio can be achieved with -10V bias and 19pJ pump energy. This device is predicted to reach 5GBit/s with 2.2pJ pump energy. Both Xu [12] and Preble [13] work with an embedded p-i-n junction that does not fully encompass the ring. Speed is limited by the

difficulty of carrier extraction in the region of the ring in the proximity of the waveguide where there is no junction.

The next ring generation presented by the same group, Xu [14] improves the junction encompassing the ring: a nearly closed circular junction is formed around the ring with an additional n+ doping added outside the waveguide region, allowing for efficient carrier extraction under reverse bias. Furthermore, Xu proves the feasibility for wavelength division multiplexing applications. Four cascaded rings are fabricated on the same waveguide. Radiuses are 4.98μm, 5.00μm, 5.02μm, 5.04μm and the achieved extinction ratios are 13dB for the first two rings and less than 10dB for the second two. Modulation speed is of the order of 5GBit/s, while it is theoretically claimed it should reach 10GBit/s.

According to Xu [15], a forward biased, carrier injection based p-i-n ring modulator can achieve high bit rates (>10Gbit/s) only if the trade-off between the optical rise time and charge storage time is broken. The device used to prove this concept is the same as in [14]. Applying a high forward bias for a time shorter than the time needed for charge saturation to occur and then decreasing it to a lower value, allows to have a short rise time and a short charge storage time as less carriers are injected in the intrinsic region. Steady state charge and charge storage time depend on the lower voltage while the optical rise time depends on the higher voltage. If high forward bias pulses of ~4V are applied to each transition edge of the pseudo-random 12.5GHz bit sequence used to probe the modulator with non-return to zero signal (V_{pp} ~8V), 12.5Gbit/s modulation with ~9dB extinction ratio

is achieved. Another advantage of such a biasing scheme is that, ultimately, power consumption is also reduced thanks to the lower carrier injection into the junction.

Manipatruni models in [16] a high field transport device relying on a novel doping profile device based on a symmetric p-i-n-i-p scheme: two mirroring p-i-n diodes (Figures 1.7(a) and 1.7(b)), where one ridge is used as optical waveguide and the other one as a "charge reciprocating ring". The unipolar behavior of the design allows for the decoupling of the time response of electrons and holes, avoiding jitter effects (due to electron and hole different recombination times). As a forward bias is applied to one junction, the charge density needed to reverse bias the second p-i-n junction limits the injected charge. Instead, when a reverse bias is applied onto the first junction, the first junction will be reverse biased and it will inject carriers into the second junction accordingly. The simulated device has dimensions $<10\mu$m. If a Q=5,000 is assumed, as well as an insertion loss of 3dB, and a critical coupling condition ring loss of 8dB/cm, under an ac bias with $5V_{pp}$, the extinction ratio is 12dB with modulation speed 40Gbit/s (NRZ). Rise and fall times are 10ps and 15ps, respectively. The estimated power consumption of the device is of 2.25fJ/bit/device length.

Metal-Oxide-Semiconductor Configuration Barrios [17] (and Lipson [18]), simulates accumulation, depletion and inversion regimes of a MOS ring structure with 14μm radius. Only the first two regimes are considered adequate for optical device performance. The device reaches 5.75dB extinc-

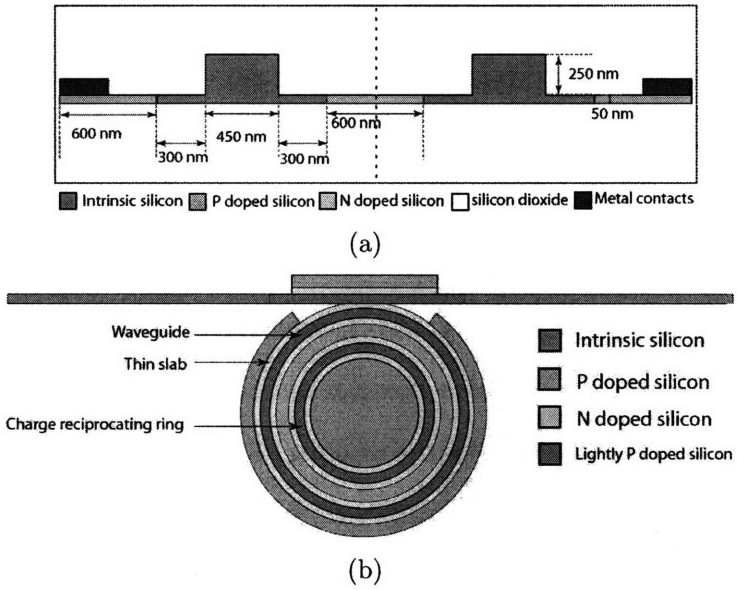

Figure 1.7: Ring modulator with an embedded p-i-n-i-p junction structure. (a) p-i-n-p junction cross-section. (b) Complete device top view: p-i-n-i-p junction embedded in the double-ridge ring modulator. Only the outer ring supports an optical mode. [16]

tion ratio and 59% transmittivity in the accumulation regime with V_{gate} of 0V in the "off" state and V_{gate} of 5V in the "on" state. In the depletion regime again with 0V of V_{gate}("off" state) and -5V V_{gate}("on" state), transmittivity reaches 23%.

1.4.2 Mach-Zehnder Structure

A Mach-Zehnder interferometer is composed of a waveguide branching out in two arms that then reunify (Figure 1.8). If a phase modulator is built in in one arm (or in both), the wave passing through one arm experiences a phase lag with respect to the other arm; interference results upon waveguide

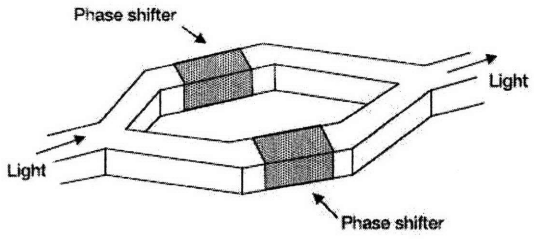

Figure 1.8: Mach-Zehnder structure showing phase shifters in the two arms, [23].

reunification. Destructive interference happens if the relative phase shift of the waves traveling in the two arms varies by exactly π radians. Phase modulation is translated to optical intensity modulation by switching between constructive and destructive interference; the transmitted intensity can be varied between "0s" and "1s".

A Mach-Zehnder device is a single-pass device. This automatically implies that a longer device is required to induce the significant modulation depth. The small effective index variation achievable in Silicon requires longer device length to induce an appreciable amount of modulation. As a general rule, the longer the arm of the modulator, the lower the required applied bias. Silicon based applications at 1550nm normally require device lengths of the order of millimeters. Despite device dimensions, the main advantage of this structure with respect to ring resonators and Fabry-Pérot cavities is that is has low sensitivity to temperature variations and broader operation wavelength.

All optical A 2mm long Mach-Zehnder modulator with either balanced or unbalanced arms is simulated by Almeida with pump and probe wavelengths of $\sim$1550nm [19]. The device relies on the plasma dispersion effect and the free carrier lifetime is estimated to be 1.4ns with a modulation time

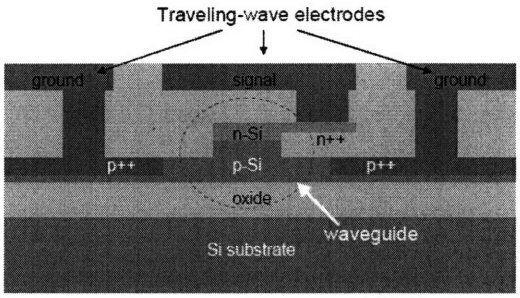

Figure 1.9: Silicon modulator based on a Mach-Zehnder interferometer with a pn junction and traveling wave electrodes. 20dB extinction ratio, f_{3dB} ~20GHz, data rate: 30Gbit/s, [20].

of 20ps; no modulation depth is reported. The same device is also fabricated: arm length of the balanced arm design is 4mm; its modulation time is 64ps. Slightly shorter is the device with unbalanced arms, 3mm with 51ps modulation time. Both devices show less than 5dB extinction ratio.

p-n and p-i-n Configurations A pn junction high speed Silicon modulator based on the carrier depletion effect is designed by Liu in [20], [21]. It is a single mode device working at 1550nm. As Figure 1.9 depicts, the p-doped Silicon rib waveguide has an n-doped Silicon cap layer. Rib width and height dimensions are $0.6 \cdot 0.5 \mu m^2$. While the p-doping profile is uniform ($\sim 1.5 \cdot 10^{17} cm^{-3}$), the n-profile is graded with lowest concentration at the pn interface (from $\sim 1.5 \cdot 10^{17} cm^{-3}$ to $\sim 3 \cdot 10^{18} cm^{-3}$). Traveling wave electrodes are used to decrease the RC limitation. This device has ~20dB extinction ratio with an insertion loss of ~7dB. The $V_\pi \cdot L$ figure of merit is ~4V·cm. Using a 1mm long phase shifter per arm, $6.6 V_{pp}$ ac signal, 3.5V dc bias, the roll-off bandwidth measures ~20GHz and data transmission rate is 30Gbit/s.

An ultra-compact Mach-Zehnder interferometer (<200μm long) with a p-i-n embedded junction on an SOI substrate is proposed by Green in [22].

The waveguide has width and height of $550 \cdot 220 nm^2$ and it lies on a 35nm Silicon layer that acts as a conductive path between the intrinsic waveguide and the heavily doped p+ and n+ regions (both having doping concentration of $\sim 1 \cdot 10^{20} cm^{-3}$). Thanks to the waveguide dimensions, both photons and injected free carriers are simultaneously confined in the intrinsic region of the junction. The overlap between the optical mode and the free carriers ensures large modulation of the modal effective index. The small waveguide dimensions also oblige large injected free carrier changes to take place mainly inside the small waveguide core cross-section. At λ=1550nm, 16GHz RC frequency cut-off is measured (200fF reverse bias capacitance). Metal contacts unintentionally placed cause 12dB of on-chip loss which in turn limits the extinction ratio to 6-10dB. Under these conditions and with a V_π=1.8V, the figure of merit is $V_\pi \cdot L$=0.36V·mm. $V_\pi \cdot L$ is given by a 200μm long phase shifter and a $\Delta n \sim 4 \cdot 10^{-3}$ modal effective index change, and an injection of free electron-hole pair density of $\sim 1.5 \cdot 10^{18} cm^{-3}$. The high frequency behavior is investigated with a $1.2V_{pp}$ non-return to zero pattern, and 3.5V peak amplitude pre-emphasis pulses. When a bias of 0.3V is applied to a 100μm long phase shifter operating at 5Gbit/s, a dc current of 2.17mA is generated corresponding to a consumption of dc power of 230μW (due to 49Ω forward resistance) and of an RF power of 41mW. The same measurement is repeated with no applied bias on a 200μm long phase shifter at 10Gbit/s. Results are: 287mA dc current corresponding to 287μW and 51mW dc and RF power consumptions, respectively. The RF power consumption requires an energy/bit equal to 5pJ/bit.

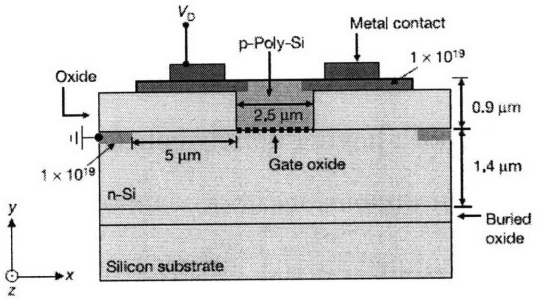

Figure 1.10: MOS capacitor cross-section from [23]. Extinction ratio of 16dB is reached with $7.7V_{pp}$, 1GHz bandwidth, modulation speed 4Gbit/s.

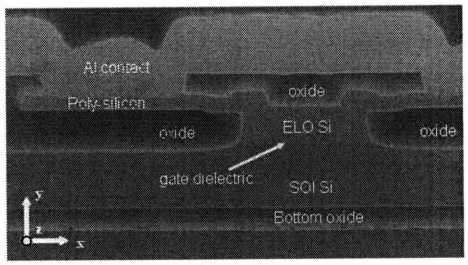

Figure 1.11: MOS capacitor cross-section from [26]. Extinction ratio of 3.8dB is reached with $1.4V_{pp}$, bandwidth 10GHz, and 10Gbit/s modulation speed.

Metal-Oxide-Semiconductor Configuration The advantage of a Mach-Zehnder with a MOS configuration under accumulation regime is that is is a majority carrier device. The device bandwidth is not limited by carrier recombination as it is the case for p-i-n junctions.

A Mach-Zehnder interferometer with a MOS structure embedded in a Silicon rib waveguide (width·rib height: 2.5·2.3 μm^2) is presented in [23], [25], and [24]. A cross-section of the MOS structure is pictured in Figure 1.10. A potential drop (applied forward bias, V_D) across the n-doped ($\sim 1 \cdot 10^{16} cm^{-3}$) Silicon layer and the p-doped ($\sim 5 \cdot 10^{16} cm^{-3}$) poly-crystalline Silicon layer forms two charge accumulation layers near the gate oxide: an electron charge layer at the n-doped Silicon-oxide interface and a hole charge layer at the p-doped Silicon oxide interface. The refractive index is modified only in the charge layers and this ultimately triggers an optical absorption change.

Modeled and measured results of an individual phase shifter reveal linear

proportionality both between the driving voltage and the experienced phase shift, and between the phase shift and the phase shifter length. The obtained figure of merit is: $V_\pi \cdot L \sim 8V \cdot cm$.

dc measurements are performed with a 10mm asymmetric Mach-Zehnder phase shifter with one MOS capacitor per arm. At 1540μm, an extinction ratio of 16dB is measured with a peak-to-peak voltage of $\sim 7.7V_{pp}$. Insertion loss is estimated as ~15.3dB (4.3dB interface coupling loss, 6.7dB on-chip loss). A Mach-Zehnder with a 2.5mm phase shifter with only one MOS capacitor is used for ac measurements. The modulation speed is studied by using either a r.m.s sinusoidal source (0.18V) or a digital pulse pattern (3.5V) at 1558μm. Enhancement of device sensitivity is obtained by applying a 3V dc bias. The measured modulation speed exceeds 1GHz (2.5GHz is claimed in [27]). 1Gbit/s data transmission is demonstrated with a 3V dc bias and a 3.5V pulse pattern and a pseudo-random electrical data input.

Improvements suggested by Liu [23] are taken into account in [26]. The poly-crystalline Silicon is replaced by crystalline Silicon grown by lateral epitaxial overgrowth (ELO), thus reducing optical losses. As phase modulation efficiency depends both on the waveguide size and charge layer thickness, waveguide dimensions are down scaled (width·rib height: $1.6 \cdot 1.6\ \mu m^2$) as well as the gate oxide thickness (from 12 nm to 10.5nm); doping concentrations are increased to achieve higher bandwidth (n-doping $\sim 2 \cdot 10^{17} cm^{-3}$ and p-doping $\sim 1 \cdot 10^{18} cm^{-3}$). $V_\pi \cdot L$ becomes 3.3V·cm and a bandwidth exceeding 10GHz is later claimed by the same author in [27].

High speed measurements are obtained by applying -3.3V dc bias to n-

doped Silicon slab, a varying dc bias to the low speed section of the modulator arm (to reach quadrature), and 1.4V ac pulses to the p-Silicon. Data transmission is as high as 10Gbit/s with 3.8dB extinction ratio. These values are still limited by the drive circuitry.

Theoretical improvements are suggested by Liao in [27]: modeling the transient response of the phase modulator, 10GHZ bandwidth is predicted with a graded doping profile. Physical length details of this structure is given in Table 1.2 as well as a comparison with the previous two MOS devices ([23], [26]).

	Liu [23]	Liao [27]	Liao [26]	Liao [27]
Publication Year	2004	2006	2005	2006
Result Type	Experimental		Experimental	Modeling
Material	c-Si(n); poly-Si(p)		c-Si(n); ELO-Si(p)	-
Waveguide Dimensions	$2.5{\cdot}2.3\mu m^2$		$1.6{\cdot}1.6\mu m^2$	$1{\cdot}1\mu m^2$
Gate Oxide Thickness	12nm		10.5nm	6nm
n-Doping	$1.7{\cdot}10^{16}cm^{-3}$		$2{\cdot}10^{17}cm^{-3}$	Graded
p-Doping	$5{\cdot}10^{16}cm^{-3}$		$1{\cdot}10^{18}cm^{-3}$	Graded
$V_\pi{\cdot}L_\pi$	~8V·cm	7.8V·cm	3.3V·cm	-
Transmission Loss/L_π	Not Specified	10dB/L_π	9dB/L_π	-
Frequency Response:				
Phase Modulator Length	10mm	2.5mm	15mm	-
3dB Bandwidth	~1GHz	>2.5GHz	10.2GHz	>10GHz
On-chip Loss	6.7dB	4dB	10dB	2dB
Total Insertion Loss	~15.3dB	Not Specified		
Data Transmission Performance:				
Total Device Length	Not Specified	15mm	15mm	-
Arm Length	Not Specified	13mm	13mm	-
Phase Modulator Length	2.5mm	3.45mm	3.45mm	-
Low-Speed Section Length	NA	4.75mm	4.75mm	-
Extinction Ratio	16dB	1.3dB	4.2dB(3.8dB)	-
dc Bias on n-Si	3V	-3.3V	-3.3V	-
ac Bias on Phase Modulator	3.5V	1.4V	1.4V	-
Bias on Low-Speed Section	NA	Not Specified	Not Specified	-
Rise Time	Not Specified	82ps	57ps(55ps)	-
Bit Rate	1Gbit/s	4Gbit/s	6Gbit/s(10Gbit/s)	-

Table 1.2: Intel's MOS capacitor Mach-Zehnder structure evolution. The second (Liu [23]) and third column (Liao [27]) are two different descriptions of the same device. Fourth and fifth represent experimental (Liao [26]) and modeling (Liao [27]) improvements. (NA = not applicable)

1.4.3 Fabry-Pérot Interferometers

All Optical Modulation A fabry-Pérot structure relying on all optical modulation is demonstrated in [28]. The input optical signal is modulated by variation of the optical pumping source. The cavity acts as an amplifier, hence allowing for a non-local optical power source.

p-i-n Configuration A free carrier dispersion effect based Fabry-Pérot cavity with distributed Bragg reflector microcavities is simulated by Barrios [29]. The device length is 20μm and it is optimized to work at 1550nm. It is a single mode device with optical confinement ensured by distributed Bragg reflector microcavities and the Fabry-Pérot cavity itself, and with electrical confinement ensured by a side trench etched p-i-n structure. Static response of the device is characterized by 6.9dB extinction ratio and 87% transmittivity obtained with a bias of 0.87V, an optical input power of 25μW, and 116A/cm^2 drive current. The dynamic response is simulated with 300ns pulses for both the "on" state (0.87V) and the "off" state (-5V). Calculated rise time is 14ns, 1.25ns fall time, and 16ns switching time. Simulations show no significant thermo-optic effect.

An improved similar structure is modeled in [30]. Again based on the free carrier dispersion effect, this time it is a straight rib waveguide intensity modulator with a one dimensional photonic crystal structure embedded in a cavity 10μm long. Static response shows theoretical extinction ratio of 6.9dB achieved with 0.87V and an input optical power of 1.53μW/μm and a driving current of 1.67μA/μm. The dynamic response is measured as in the previous

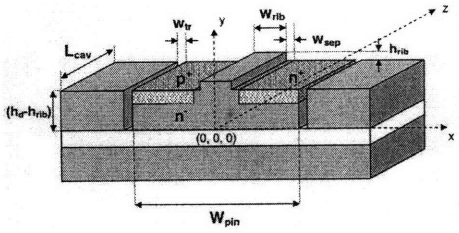

Figure 1.12: p-i-n Fabry-Pérot microcavity with distributed Bragg reflectors. 20μ long, 6.9dB extinction ratio with 0.87V, [29]

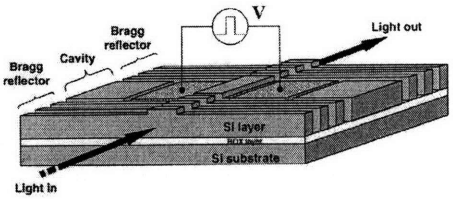

Figure 1.13: Improved design of the p-i-n Fabry-Pérot microcavity. 10μm long, 6.9dB extinction ratio with 0.87V, [30]

device: 300ns pulses for both "on" state and "off" state voltages of 0.87V and -5V, respectively. The rise time is 1.11ns and the fall time is 0.18ns, while the switching time is 1.3ns. The major achievements of this newly proposed structure are the switching time improvement and the dimension shrinkage.

Schmidt presents in [31] an ultra-small Fabry-Pérot cavity embedded in a high index contrast Si/SiO_2 waveguide with five periodic holes on either side of the cavity forming a distributed Bragg reflector. Holes have 220nm diameter and 420nm spacing. The cavity is 2.51μm long, while the total device length including the holes is <6μm. Based on free carrier dispersion, the cavity is the intrinsic layer of a p-i-n junction and the p and n lie on the sides of the cavity, as depicted in Figure 1.15. With 5.6V dc bias, a modulation depth of 5.93dB is achieved at λ=1568nm. The insertion loss is 5.1dB, coupling and waveguide losses combined are 23.5dB. $Q_{experimental}$ measures $\sim$ 253, while $Q_{theoretical}$ $\sim$780. Such a difference is due to sidewall scattering and device design sensitivity to fabrication. When 0.7V dc bias is applied in conjunction with an ac swing of $2.0V_{pp}$, the extinction ratio

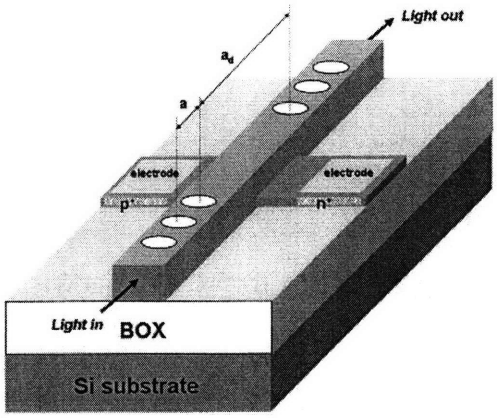

Figure 1.14: 3-dimensional full structure of the improved design of the p-i-n Fabry-Pérot microcavity with distributed Bragg reflectors. 10μm long, 6.9dB extinction ratio with 0.87V, [30]

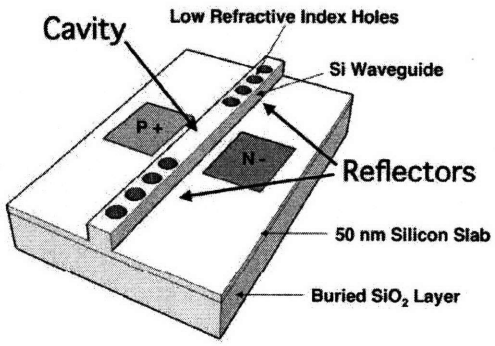

Figure 1.15: Fabry-Pérot microcavity (<6μm) with distributed Bragg reflector structure and embedded p-i-n junction. Low frequency measurements show 5.93dB modulation depth with 5.6V dc bias; maximum data transmission speed is 250Mbit/s with 5.87dB extinction ratio with 0.7V(dc) and $2V_{pp}$(ac), [31].

is 5.87dB and the transmission speed is 250Mbit/s. Rise and fall times are 2.27ns and 1.96ns, respectively. It is claimed that if $Q_{experimental}$ could equal $Q_{theoretical}$, the modulation speed would be ~1Gbit/s, with a dc bias of only 0.3V.

1.5 Summary

As modulators are becoming key building blocks in the electronic-photonic integration, the need to fulfill small footprint, low driving voltage, large modulation depth and high speed requirements becomes fundamental. This first

chapter summarizes light modulation physical principles. Electro-optic, carrier injection and depletion, thermo-optic and all-optical mechanisms are reviewed. These mechanisms are then combined to optical structures. Non-biased devices as well as p-i-n structures or MOS configurations are explored through a partial literature review of Silicon based devices operating operating at 1550nm.

Ring modulators, Mach-Zehnder interferometers and Fabry-Pérot cavities are the three main structures used for Silicon based modulators operating at 1550nm. The key advantage of ring modulators is their small footprint, but they are highly temperature sensitive and they are not broad band devices. Instead, Mach-Zehnder devices have larger wavelength range of operation; they are tolerant to small temperature differences but they have large footprint. Published results on Fabry-Pérot based modulators always exploit the use of photonic cavities which are highly sensitive to fabrication and temperature variations.

Chapter 2

Device Physics, Material's Choice, Design, and Fabrication

Key guiding parameter to keep in mind while reading this chapter is the figure of merit of the device being studied. The optimization of such parameter, $\Delta\alpha/\alpha_{on}$ (i.e. the ratio between the modulation depth and the insertion loss) is of key importance while considering the physical mechanism leading to modulation and the choice of the material of the device.

This chapter explains the theoretical background and the alloy composition choice on which the final working device relies. The modulator butt-coupled to high index contrast waveguides and based on the Franz-Keldysh effect to produce modulation is a novel device. Theoretical calculations of this Si_xGe_{1-x} butt-coupled modulator to Si/SiO_2 waveguides predict 10dB modulation depth with a 3dB frequency higher than 100GHz. The only expected speed limitation is the RC delay: in fact, the Franz-Keldysh effect operates in the picosecond time frame.

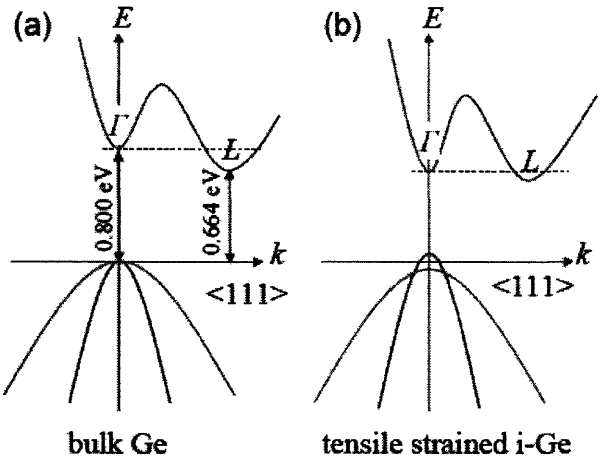

Figure 2.1: Elemental Germanium band gap diagram. (a) Bulk Germanium; (b) tensile strained intrinsic Germanium: the direct bad gap (E_g^{Γ}) decreases under the effect of tensile strain, [32].

2.1 Material's Choice Overview

In unstrained, crystalline Silicon, the linear electro-optic effect (Pockels effects) is nonexistent; the non-linear electro-optic effect (Kerr) and the electro-absorption effects (Franz-Keldysh) are weak. Moreover, its direct band gaps lie in the range 3-4eV. Not having all these challenges, Silicon would be perfect for monolithic integration on a CMOS platform because it would enable the integration of photonic devices with microelectronics.

Bulk Germanium, with its direct band gap value (0.8eV) and its higher electron (3900 $cm^2/s{\cdot}V$) and hole (1900 $cm^2/s{\cdot}V$) mobilities with respect to Silicon, is a more favorable candidate for faster devices that operate at lower power.

During epitaxial growth, Germanium is fully relaxed on Silicon; at room temperature, thermal mismatch generates tensile strain. As a result, the band gap energy of the material decreases (Figure 2.1) and becomes optimized for the wavelength window of 1633-1650nm, [32]. The addition of a

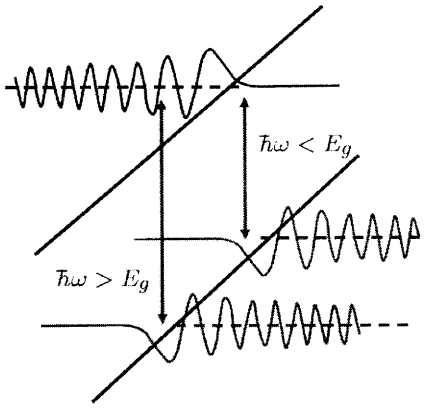

Figure 2.2: Schematic diagram representing the Franz-Keldysh effect. The band diagram tilting, due to an applied electric field, generates a finite tunneling probability for photon energies ($\hbar\omega$) smaller than the band gap (E_g) value.

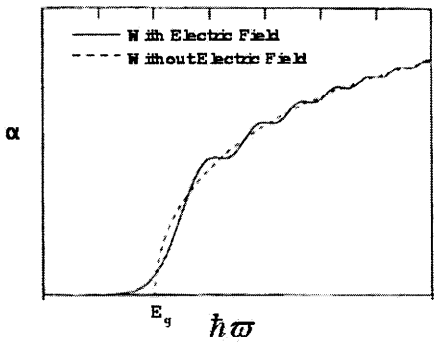

Figure 2.3: Franz-Keldysh effect: absorption coefficient (α) versus photon energy ($\hbar\omega$). The weakly absorbing regime is just below the band gap value, E_g.

small amount of Silicon increases the Germanium band gap and the direct band gap (E_g^{Γ}) can be tailored to be equivalent to the wavelength of 1550nm. Enhanced Franz-Keldysh effect in tensile strained Si_xGe_{1-x} epitaxially grown on Silicon wafers is observed [32]. Depending on the strain, the direct band gap wavelength range varies between 1550nm and 1610nm; while the indirect band gap is ~1900nm and it is less sensitive to strain.

2.2 Franz-Keldysh Theory

The absorption coefficient depends on the applied electric field and on the photon energy. As an electric field is applied, the conduction and valence

bands tilt. Their respective evanescent wave function tails extend into the band gap generating a finite probability of tunneling (Figure 2.2).

For photon energies with $\hbar\omega < E_g^{\Gamma}$ (E_g^{Γ} being the direct band gap value), the absorption coefficient increases with the applied field as the band tilt steepens. While for photon energies with $\hbar\omega > E_g^{\Gamma}$ the absorption coefficient oscillates depending on the constructive or destructive interference of the wave functions of the conduction band with the one of the valence band. These Franz-Keldysh oscillations are caused by the overlap of the wave functions inside the conduction and valence bands under a specific electric field and varying photon energies as plotted in Figure 2.3.

Referring to the figure of merit of the electro-absorption modulator being optimized, in the weakly absorbing regime, when the photon energy $\hbar\omega$ is only slightly smaller than the value of the direct band gap E_g^{Γ}, the insertion loss is reduced because the indirect gap has only a weak absorption contribution. The modulation depth, $\Delta\alpha$, is maximized if $\hbar\omega$ is close to the band edge ($\sim E_g$). For this reason, photon energies slightly below the direct band gap are expected to optimize the figure of merit.

The key idea of the Franz-Keldysh effect is the addition of a uniform electric field term in the time-independent Schrödinger equation for an electron hole pair. A few approximations can be performed: first, the uniformity of the field across the material is assumed thanks to the geometry and dimension of the device being studied. Coulombic interactions of the electron hole pair can be neglected as the electric field effect dominates on the exciton effects. This is true only in the case of photon energies smaller than the

band gap value, and it is indeed the photon energy range of interest since the Franz-Keldysh effect of the weakly absorbing regime is the one exploited in these electro-absorption modulators. Another important approximation while solving the Schrödinger equation is the assumption that only electrons and holes that reside near the conduction and valence band edges take part in the band to band transitions.

The solution to the Schrödinger equation written with these approximations, the total wave function, is then inserted in the absorption coefficient, $\alpha(\omega)$, derived from Fermi's Golden Rule. The applied electric field directly modifies the absorption coefficient of the material.

A detailed mathematical formulation of the solution to the Schrödinger equation and absorption coefficient calculation can be found in Chuang [35] and summarized in Liu [36].

2.3 Si_xGe_{1-x} Alloy

As previously mentioned, tensile strained Germanium has a band gap equivalent to the wavelength range 1633-1650nm depending on the strain level. The addition of Silicon in forming Si_xGe_{1-x} alloy offers the freedom of band gap adjustment to a predetermined value. In the case of the Si_xGe_{1-x} alloy, as the applied electric field tilts the band structure, both the direct and the indirect band gap values are affected. By increasing the Silicon content, the direct and indirect bands get further apart and the material tends to behave as indirect deteriorating its optical properties.

2.3.1 Absorption Coefficient Optimization

The theoretical modeling of the electro-absorption properties of the material is done using the generalized Franz-Keldysh theory proposed by Shen and Pollak in [33]. As the Franz-Keldysh effect is found to be strongest in the direct band gap, the indirect band gap contribution is neglected [34].

Their proposed theory requires the a priori knowledge of four material parameters: the direct band gap value, effective electron and hole masses, the real part of the refractive index, and the optical transition matrix element. The four material parameter are evaluated as follows:

1. The direct band gap value depends on the Silicon concentration in the alloy and on the thermally induced strain.

   Direct Band gap Calculation with no Tensile Strain:

   Theoretical absorption calculations in the weakly absorbing regime are performed by first understanding the approximate Silicon concentration needed, then including strain effects in the calculations.

   When it is assumed there is no strain, the Si_xGe_{1-x} direct energy gap can be inferred by linear interpolation between the pure Silicon (4.06eV at room temperature) and the pure Germanium with the following [38]:

   $$E_g^{\Gamma}(Si_xGe_{1-x}) = 0.80 + 3.26 \cdot x$$

   According to this formula a Silicon dilute concentration of <2% is required to achieve the targeted wavelength of 1550nm. In the same way,

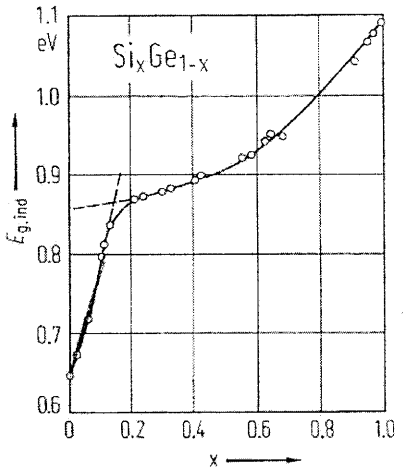

Figure 2.4: Si_xGe_{1-x} indirect bad gap dependence on Silicon concentration. For x<15% the relation is linear, [40].

linear interpolation in the regime 0-15% (Figure 2.4) can be used to calculate the indirect Si_xGe_{1-x} band gap, [39]:

$$E_g^L(Si_xGe_{1-x}) = 0.66 + 1.2 \cdot x$$

Band gap Calculation including Tensile Strain:

The first consideration regards the shape of the device. While a blanket layer of Si_xGe_{1-x} grown on a Silicon substrate would have isotropic in-plane strain, due to the trench-growth, elongated shape of the device, it is found that the material is fully relaxed in the transverse direction and it is strained in the longitudinal one (i.e. the light propagation direction) [36]. Trench growth is used for two reasons. First it improves coupling losses. Secondly, a single-mode device is obtained only with a cross-section smaller than $1{\cdot}1\mu m^2$ and device length of the order of tens of microns to ensure high modulation depth.

Experimental and theoretical selective trench growth details with Borgstrom and Wulff construction as well as strain explanation and detailed calculations can be found in Ref. [36].

Once the tensile strain is determined, formulae for the light hole, heavy hole and split off band gaps can be found in the literature [37]. They imply the knowledge of deformation potentials and elastic constants, which can be determined by linear interpolation between Silicon and Germanium.

2. The refractive index can also be found by linear interpolation according to [41]:

$$n(Si_xGe_{1-x}) = 4.10 - 0.64 \cdot x$$

3. Effective electron and hole masses of pure Germanium are used, as the Si_xGe_{1-x} ones with x<0.02 are experimentally undistinguishable from pure Germanium [42].

4. The transition matrix element for the direct band gap of Si_xGe_{1-x} is extrapolated from k·p theory.

Once these four material parameters are numerically defined, the Franz-Keldysh effect can be modeled and optimized with respect to Silicon concentration.

Simulation iterations with increasing Silicon (0.5%-1.1%) concentration show that the band gap shifts from 1570nm to 1530nm [36]. As Silicon is added, the material starts behaving as if it had an indirect band gap,

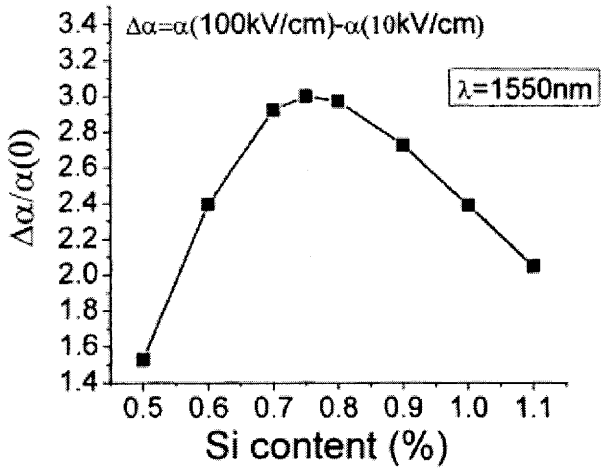

Figure 2.5: Figure of merit optimization with respect to Silicon content in the Si_xGe_{1-x} alloy [36].

consequently deteriorating its optical properties. The physical reason is that the Franz-Keldysh effect due to the direct band gap becomes insignificant, while the one due to the indirect band gap absorption prevails.

As is seen in Figure 2.5, at the optical "off" state with an applied electric field of 100kV/cm, the figure of merit $\Delta\alpha/\alpha_{on}$ at 1550nm is maximized for Silicon concentrations in the range 0.7-0.8%, where the value reaches ~3.0. This translates to an extinction ratio of 12dB, assuming an insertion loss of 4dB. The maximum device length allowed in order to achieve an insertion loss <4dB is 70μm and it is found by studying the absorption coefficient as a function of applied electric field in the range 0-130kV/cm [36].

2.4 Device Design

The device experimentally analyzed in the next chapter is designed by Liu [36]. The following is intended to highlight the main points of the design and fabrication.

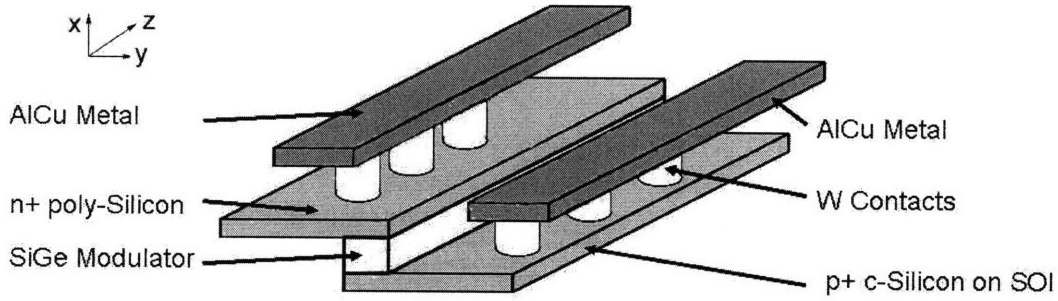

Figure 2.6: 3-D representation of the Si_xGe_{1-x} modulator, the two Silicon layers (n+ and p+ regions of the p-i-n junction), and electrodes (W contacts and AlTi metal layers). Silicon waveguides (not pictured) couple in and out directly from the Si_xGe_{1-x}. Design not in scale.

The complete design includes the Si_xGe_{1-x} modulator as well as the waveguides used to couple light in and out of the device. The novelty of the structure relies on the butt-coupling scheme. A schematic representation of the structure is in Figure 2.6 and the waveguide-modulator coupling is shown in Figure 2.7. Tapered crystalline Silicon waveguides are evanescently coupled to tapered amorphous Silicon waveguides. The amorphous Silicon waveguides butt-couple light into the modulator.

The key idea of the butt-coupling design is that the center of the input (output) waveguide terminates (begins) in the center of the Si_xGe_{1-x} cross-section perpendicular to the light propagation direction.

Waveguide and modulator designs will be considered first; attention will then be focused on the complete structure in order to maximize the figure of merit.

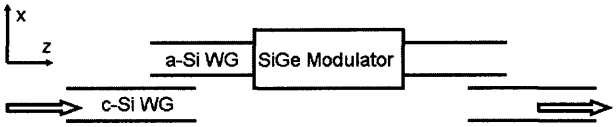

Figure 2.7: 2-D longitudinal cross-section of the butt-coupled Si_xGe_{1-x} modulator with a-Silicon waveguides. Tapered waveguides are used to enhance coupling efficiency. Design not in scale.

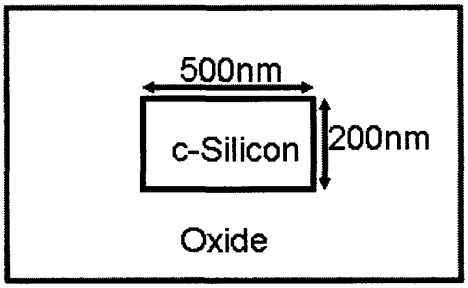

Figure 2.8: High-index contrast Si/SiO_2 waveguide cross-section. Core dimensions used are indicated in the figure. Figure not in scale.

2.4.1 Si/SiO_2 Waveguide

A single mode Si/SiO_2 high index contrast waveguide (Silicon refractive index: 3.48; SiO_2 index: 1.46) is used as bus to couple light into the modulator. The width of the Silicon core is 500nm, and its thickness is 200nm. These dimensions ensure single mode operation. An oxide overcladding on the waveguide is assumed for simulation purposes and light leakage to the substrate is avoided thanks to the incorporation of a thick oxide layer (3μm) underneath the Silicon layer. A waveguide cross-section is shown in Figure 2.8.

Both TE (where the electric field polarization is parallel to the substrate) and TM (where the electric field is perpendicular to the substrate) modes are evaluated. A higher confinement factor is found in the case of TE polar-

Si/SiO_2 Waveguide Parameters (1550nm)	TE	TM
Effective Index	2.443	1.737
Confinement Factor	0.825	0.524
Bending Loss (2μm Bending Radius)	2.1dB/cm	1346dB/cm

Table 2.1: Si/SiO_2 waveguide calculation results at 1550nm after [36]

ization, which ensures lower bending losses and hence higher on-chip packing densities. For the purpose of on-chip integration this concept is of fundamental importance and hence the device structure will be optimized for TE polarization. Table 2.1 shows a comparison between simulated parameters for TE and TM fundamental modes.

2.4.2 Si_xGe_{1-x} (x = 0.75%) Electro-absorption Modulator

The following structure is considered for simulation purposes (Figure 2.9): a 200nm thick crystalline Silicon layer with $2{\cdot}10^{19}/cm^3$ p+ doping concentration as undercladding; a 400nm high, and 600nm wide Si_xGe_{1-x} intrinsic region; and a polycrystalline Silicon top cladding 200nm high with $2{\cdot}10^{19}/cm^3$ n+ doping concentration. As in the case of the waveguide, leakage to the substrate is prevented with a 3μm SiO_2 undercladding. Maximum device length is 70μm, to obtain an insertion loss lower than 4dB. Table 2.2 shows simulation results of such a device.

Si_xGe_{1-x} Parameters (1550nm)	Optical State	TE	TM
Effective Index		3.71	3.728
Confinement Factor		0.886	0.881
Imaginary Effective Index	"on" state, 0V	0.00210	0.00210
Modal Absorption Coefficient	"on" state, 0V	170/cm	170/cm
Imaginary Effective Index	"off" state, -3.3V	0.00767	0.00733
Modal Absorption Coefficient	"off" state, -3.3V	622/cm	594/cm

Table 2.2: Optical mode evaluation. TE versus TM fundamental modes in Si_xGe_{1-x} device. Data after [36]

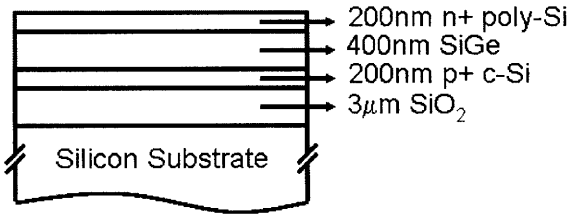

Figure 2.9: Si_xGe_{1-x} electro-absorption modulator cross-section. Design not in scale.

2.4.3 Figure of Merit Optimization

At the beginning of this chapter, $\Delta\alpha/\alpha_{on}$, i.e. the ratio between the modulation depth and the insertion loss, is mentioned. In terms of material parameters this expression becomes:

$$\frac{ExtinctionRatio}{InsertionLoss} = \frac{\kappa_{absorption}(V \neq 0) - \kappa_{absorption}(V = 0)}{\kappa_{absortpion}(V = 0) + \kappa_{coupling}}$$

All these parameters are here evaluated while the design device is being optimized.

Insertion Loss The insertion loss is given by the sum of the absorption loss ($\kappa_{absorption}$) at the optical "on" state and the coupling loss ($\kappa_{coupling}$):

Absorption Loss It depends on the Si_xGe_{1-x} modal absorption coefficient when no bias is applied, α_{mod}(V=0):

$$\text{Absorption Loss} = \kappa_{absorption}(V = 0) = \text{-}10 \cdot \log\left\{e^{-\alpha_{mod}(0) \cdot L}\right\},$$

where L is the modulator length. In turn, the modal absorption coefficient is related to the absorption coefficient of the Si_xGe_{1-x} and neighboring Silicon cladding layers and on the amount of optical power in them.

Coupling Loss Total coupling loss is given by modal dispersion (in the direction perpendicular to the direction of propagation), and reflection losses (in the propagation direction) between the Silicon waveguide and the Si_xGe_{1-x} device.

Coupling losses between the waveguide and the modulator and back to the waveguide can be decreased with the butt-coupling design. The mode overlap is enhanced when the waveguide and the modulator are butt-coupled but it is also a function of device dimensions. The overlap can be studied as a function of device height while keeping the Si_xGe_{1-x} width fixed (600nm). Lower mode mismatch is found for thinner Si_xGe_{1-x} thickness, which leads, consequently, to higher coupling efficiency. On the other hand, the confinement factor is also a function of device height: it increases as the device height becomes thicker. The intersection of these two trends (Figure 2.10) leads to a trade-off between an optimized confinement factor in the Si_xGe_{1-x} layer and a maximized mode overlap between the Si/SiO_2 and the Si_xGe_{1-x}.

While considering the overall device performance, general rules are: as the mode overlap improves (i.e. thinner Si_xGe_{1-x} layer), the confinement factor

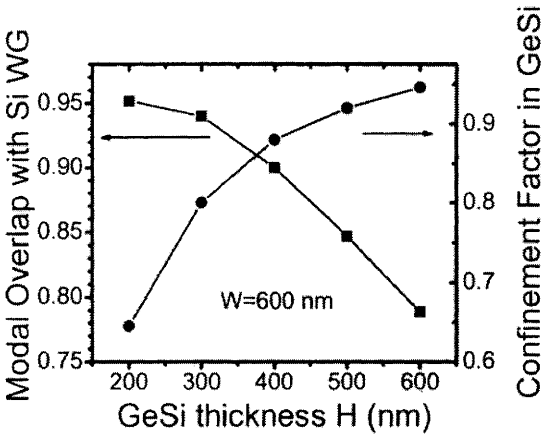

Figure 2.10: Trade-off between the modal overlap in the Silicon waveguide and the confinement factor in the Si_xGe_{1-x} layer [36].

worsens. Since only the light that is physically inside the Si_xGe_{1-x} layer can be modulated, a higher confinement factor is desirable. Also, as the Si_xGe_{1-x} layer becomes thinner, at the optical "on" state (0V) the built-in electric field increases, drastically decreasing the absorption coefficient. The absorption coefficients of the optical "on" and "off" states become less far apart. Therefore, the achievable modulation depth decreases. A comparison between a 600nm and a 200nm thick layer is reported in Table 2.3. The estimated total coupling loss is as low as ~1dB.

Extinction Ratio It is given by the difference between the absorption loss of the Si_xGe_{1-x} as a bias is applied to the device, $\kappa_{absorption}(V \neq 0)$, and the absorption coefficient when no bias is applied, $\kappa_{absorption}(V = 0)$:

$$\text{Extinction Ratio} = \Delta\alpha_{mod} = \kappa_{absorption}(V \neq 0) - \kappa_{absorption}(V = 0).$$

Scanning the Si_xGe_{1-x} thickness while keeping the width constant, for a device length of 50μm, an optimal thickness is found. This thickness is 400nm, independently of the device width, as shown in Figure 2.11.

Si_xGe_{1-x} Thickness	600nm	200nm
Confinement Factor	0.926	0.625
Built-in Electric Field, "on" state (0V)	7.5kV/cm	22.5kV/cm
Absorption Coefficient	140/cm	254/cm
$\Delta\alpha/\alpha_{on}$	3.5	1.5
Reflection Loss	0.2dB	0.13dB
Modal Loss	0.9dB	0.43dB
Total Coupling Losses	1.1dB	0.56dB

Table 2.3: Parameter dependence on Si_xGe_{1-x} thickness. Parameters calculated at 1550nm. After [36].

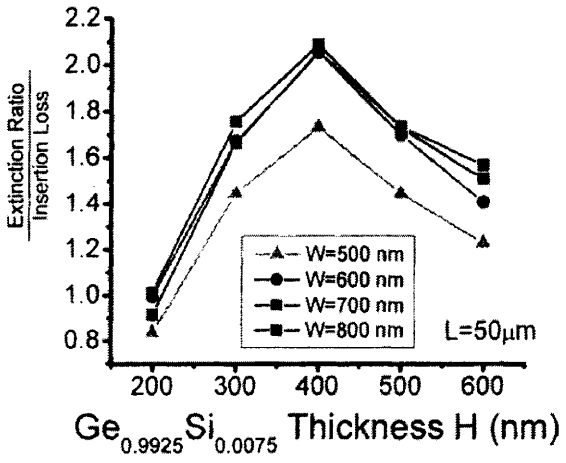

Figure 2.11: Figure of merit optimization with respect to the Si_xGe_{1-x} modulator layer thickness; various Si_xGe_{1-x} widths are considered while length is kept constant (50μm) [36].

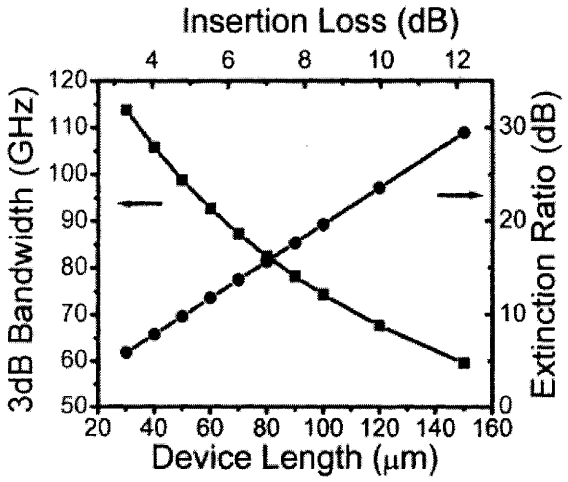

Figure 2.12: Trade-off between 3dB bandwidth, extinction ratio and Si_xGe_{1-x} modulator length [36].

For a thinner device layer, the confinement factor is too small and the modulation depth is reduced; for a thicker layer, the modal overlap decreases and the built-in electric field decreases. Another plot of interest (Figure 2.12), is device length optimization versus both 3dB frequency and extinction ratio. The 3dB frequency is highest for shorter devices where it can theoretically reach ~100GHz. As the Franz-Keldysh effect takes place in the picosecond time scale, the only speed limitation would be the RC delay of the device. A trade-off between device length, which would ensure high extinction ratio, but also high insertion loss and low 3dB bandwidth is unavoidable.

Concluding remark is that the optimization of the figure of merit of the electro-absorption modulator highly depends on material properties, confinement factors (Γ_{SiGe}, Γ_{c-Si}, $\Gamma_{poly-Si}$), absorption coefficients (α_{SiGe}, α_{c-Si}, $\alpha_{poly-Si}$) and modulator physical dimensions (height, H, width, W, and length, L) of the device. The dependence of these parameters is schematically shown in Table 2.4.

Parameters influencing FOM	α_{SiGe}	$\alpha_{poly,c-Si}$	Γ_{SiGe}	$\Gamma_{poly,c-Si}$	H	W	L
$\alpha_{mod}(0), \alpha_{mod}(V)$	x	x	x	x	x	x	
Modal overlap			x	x	x	x	
Reflectance					x	x	x

Table 2.4: Modal absorption, modal overlap and reflectance influence extinction ratio and insertion loss. Crosses indicate the dependence of these three parameters on the variables influencing the figure of merit. H,W, and L are height, width, and length of the Si_xGe_{1-x} layer.

2.5 Device Fabrication

The Si_xGe_{1-x} butt-coupled waveguide-modulator structure fabrication process is explained with the aid of Figure 2.13-2.19. Fabrication is performed on a 180nm line at BAE Systems. A cross-section of the final device is shown in Figure 2.20.

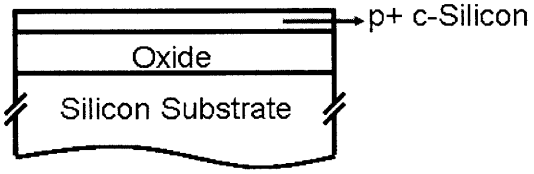

Figure 2.13: The process start with an SOI substrate. Optical isolation from the substrate is thus ensured. The oxide layer is 3μm thick. The crystalline Silicon layer is doped p+ by ion implantation.

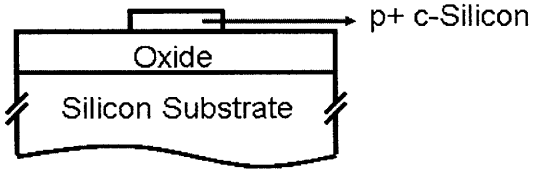

Figure 2.14: The c-Silicon p+ Boron doped layer is patterned and mesas are formed. The mesas are the p+ region of the p-i-n junction of the device.

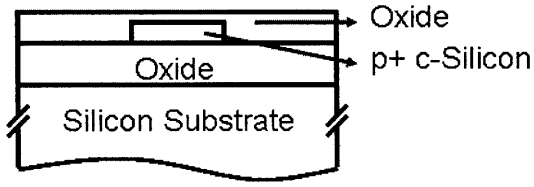

Figure 2.15: An oxide deposition follows. The obtained ondulated layer is planarized with chemical mechanical polishing (CMP).

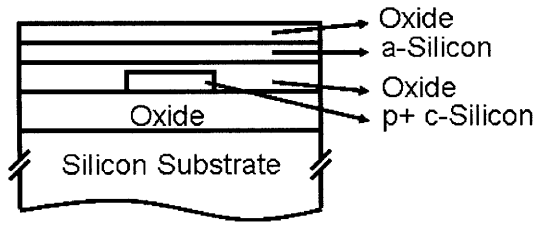

Figure 2.16: Amorphous Silicon is then deposited and patterned. This step forms the core of the amorphous Silicon waveguides. Another oxide deposition and planarization form the upper cladding of this waveguide.

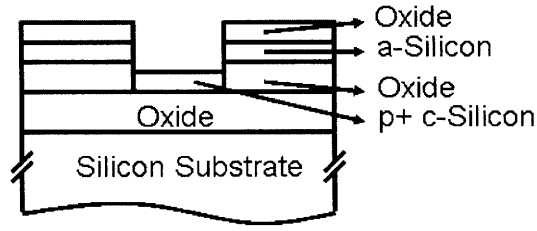

Figure 2.17: Once the waveguide structure is defined, standard photolithograpy steps are performed to open a trench that exposes the p+ c-Silicon mesa.

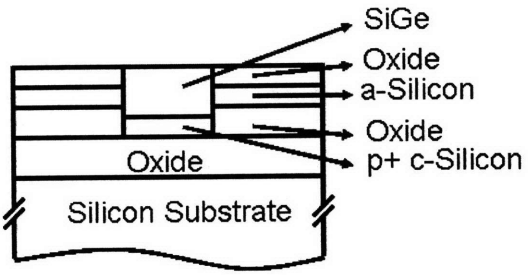

Figure 2.18: As the trench is opened, epitaxial Si_xGe_{1-x} is grown selectively between the input and output of the amorphous Silicon waveguides. The trench is purposely overfilled then planarized.

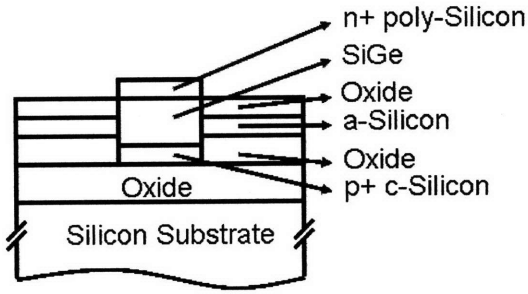

Figure 2.19: The last step is poly-Silicon deposition, n+ Phosphorous implantation, then patterning. Tungsten and AlTi metal deposition to form vias and contact pads, respectively.

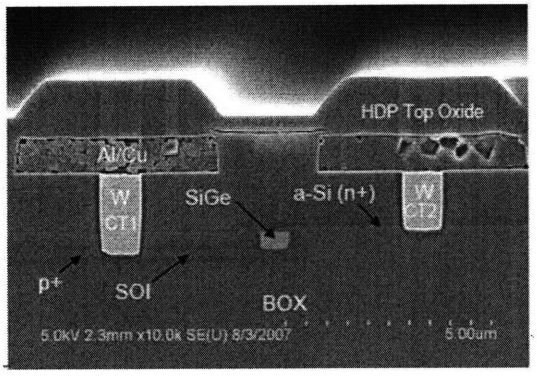

Figure 2.20: Fabricated Si_xGe_{1-x} device cross-section. The SiGe modulator is indicated in the middle of the figure. The bottom oxide layer, the p+ and n+ Silicon layers as well as the metal contacts are indicated.

2.6 Summary

This chapter reviews the design of the Si_xGe_{1-x} electro-absorption modulator butt-coupled to high index contrast Si/SiO_2 waveguides. It starts with a theoretical review of the Frank-Keldysh effect. This theory is then applied to evaluate material absorption properties of the alloy used for the design of the modulator. A Si_xGe_{1-x} alloy with a Silicon concentration of x=0.75% and with 0.2% tensile strain is chosen in order to optimize the device performance at 1550nm. Performance optimization with respect to the figure of merit of the modulator (the ratio between the extinction ratio and the insertion loss) involves also the physical dimensions of the device. The final design has height and width of 400nm and 600nm, respectively, while the length ranges between 30 and 500μm. Last, the fabrication process flow is illustrated.

The device experimentally presented in the next chapter has a length of 50μm. The expected 3dB frequency is $\sim$100GHz, with an extinction ratio of $\sim$10dB and an insertion loss smaller than 5dB.

Chapter 3

Experimental Results and Analysis

The first Si_xGe_{1-x} electro-absorption butt-coupled modulators are measured in [36]. Improvements in the fabrication process flow as well as in the coupling design are the enabling factors that permitted to perform the measurements here described. Improvements still need to be undertaken. Metallization-related issues are the major contributors to low yield: devices that are both electrically and optically active are a rarity. Nonetheless, devices that have diode behavior and are optically transparent represent a breakthrough in modulator design and performance.

The device layout used is depicted in Figure 3.1. Two sets of devices are pictured divided by a waveguide with no devices on it. In the top device series, there are modulators integrated with photodetectors. For modulators with lengths shorter than 90μm, photodetectors are all 120μm long, while for modulators 120 and 150μm long, photodetectors are 150μm long. The second series, instead, shows one modulator per waveguide; each modulator

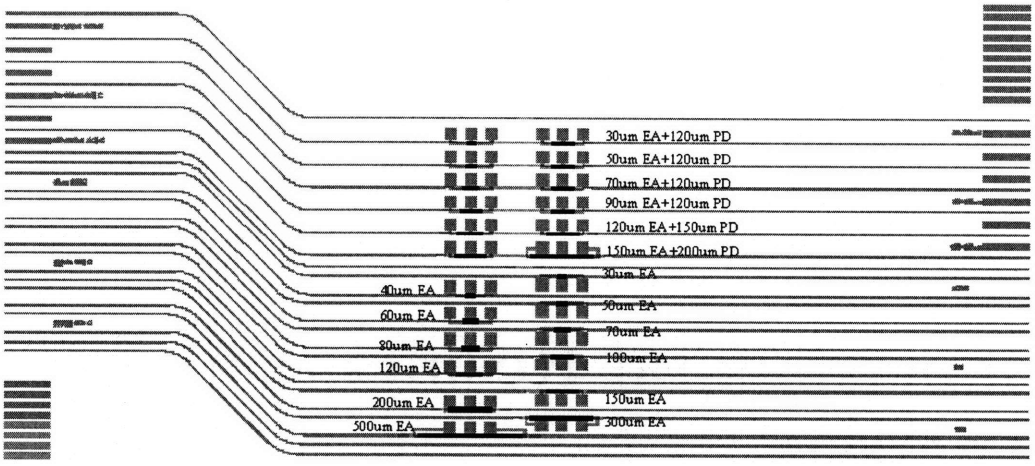

Figure 3.1: Device layout. Two sets of devices are shown: in the top set, modulators are integrated with photodetectors; in the bottom set, there is one modulator per waveguide.

has a different length (30-500μm). Important feature of this layout is that modulators and photodetectors are integrated on the same waveguide.

In the experimental description that follows, only the performance regarding modulators will be presented. As in the laboratory, electrical testing is performed first, followed by optical measurements, the same will be done here: the first section is on current-voltage (IV) results, while the second section is on low frequency (dc) measurements, followed by high frequency measurements.

3.1 IV Characteristics

Electrical probing is performed in the range -3.3, 5V as shown in Figure 3.2. Two wafers are probed (1776 devices per wafer divided in 33 dies): one single device showing diode behavior is found on the first wafer, all other devices

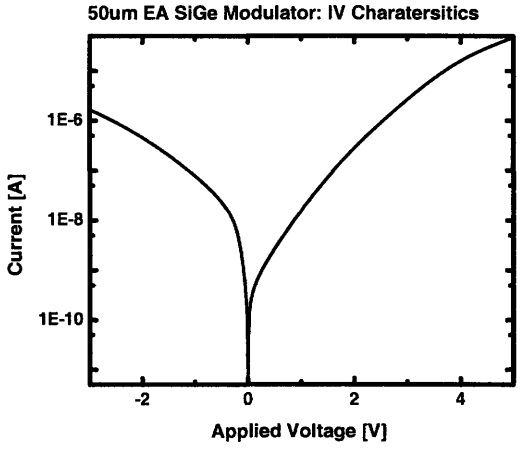

Figure 3.2: IV characteristics of the 50μm long electro-absorption Si_xGe_{1-x} modulator.

behave as open circuits. The second wafer has six dies that have devices showing diode behavior even though they have high series resistance.
Among the electrically active devices that have diode behavior, the ones on dies with highest yield and lowest resistance are used to measure modulation depth. Other devices have lower current flow (in the nanoAmpère range for a forward bias of 3V).

As the standard diode model does not fit accurately the IV data, fabrication issues need to be closely considered in understanding the IV behavior of the devices. The high series resistance is due to over-etching during fabrication of the metal contacts. Figure 3.3 shows that the silicide layer is missing underneath the Tungsten. However, the measured series resistance is of the order of 20-30kΩ and an expected speed of 1-1.5GHz can be inferred for devices with a length of 30-50μm.

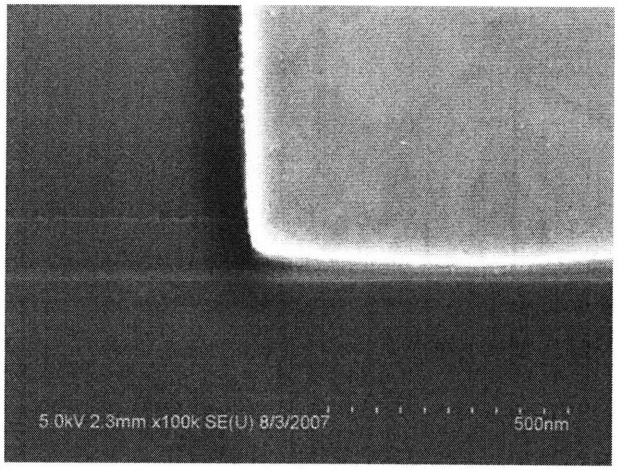

Figure 3.3: SEM image of the Tungsten contact. The silicide layer is completely missing and over-etching of the Silicon layer is clearly seen.

3.2 Low Frequency Measurements

The experimental set-up used for dc measurements is schematically pictured in Figure 3.4. A Newport continuous wavelength laser source is used for wavelengths in the range 1470-1570nm. Light from the fiber is directly coupled to the waveguide; transmitted light is also directly coupled to a fiber. This type of coupling drastically reduces scattering losses compared to free space coupling. Light is then routed to a photodetector connected to a power meter which feeds back into a lock-in amplifier. The lock-in amplifier is connected to a pulse generator that determines the applied electrical bias on the modulator through a bias tee.

Preliminary results on a first device show 30% modulation depth around 1560nm. A linear response between 5.2 and 6.5V, with a linearity factor of 13% modulation depth per applied volt, is measured. A maximum of 18% modulation depth is obtained in this linear regime.

The modulation depth is given by the ratio between the "on" and "off"

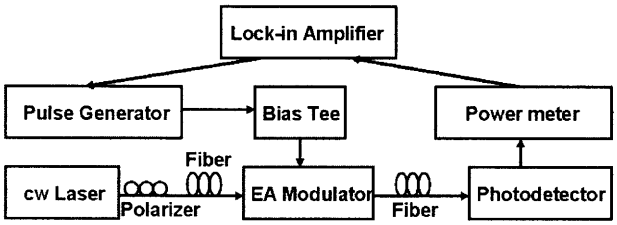

Figure 3.4: Schematic experimental set-up for dc measurements.

optical transmission states. Transmission scans also provide information on the Franz-Keldysh oscillations. The knowledge of both modulation depth and Franz-Keldysh oscillations allows the estimate of the electric field truly present inside the intrinsic region of the device. This extrapolated value is lower than the one expected from the technically applied bias. The cause of this difference is the high series resistance in the device. The device is expected to reach a modulation depth as high as 90% as soon as the origin of the over-etching during fabrication is clarified and avoided.

A second modulator is considered. It is 50μm long and it lies on the bottom device set of the layout previously pictured (Figure 3.1). Among all electrically active devices on the same die, it is the only optically transparent one. Even simple waveguides, normally used as test structures to measure waveguide loss and insertion loss, are opaque. No transmitted light can be measured. An explanation to this is that the metal filling used for chemical-mechanical polishing on top of the structure is actually interfering with light propagation drastically increasing waveguide losses, which are estimated to be of the order of 30dB/cm.

As the optical "on" state is considered (Figure 3.5), low transmittance below 1540nm is a result of the onset of direct band gap absorption. Above this

wavelength, the Si_xGe_{1-x} absorption is weak and it is only due to the indirect band gap. An estimate of this absorption is inferred from the magnitude of the Fabry-Pérot fringes, ~2dB.

Around 1550nm, the total insertion loss is determined to be ~3.7dB: ~2dB absorption loss due to indirect band gap and 1.7dB coupling loss between the waveguides and the modulator.

As a reverse bias is applied (Figure 3.6) and the electric field inside the Si_xGe_{1-x} layer increases, the absorption edge flattens towards longer wavelengths. Absorption above 1540nm significantly increases while the transmittance decreases.

If absorption is temperature induced, the absorption edge undergoes a shift while keeping the slope constant. As is seen in Figure 3.6, the slope decreases as the applied reverse bias increases, indicating that the experimentally measured absorption is a result of the Franz-Keldysh effect rather than thermal effects.

The technically applied reverse bias spans the range 0V-7V. As mentioned for the previous device, the electric field generated inside the intrinsic layer of the device corresponds to a lower effective applied bias. This effective bias is estimated using the Franz-Keldysh oscillations of the first device and the IV measurements of the second device. The first device is used as the second one does not show Franz-Keldysh oscillations and, hence, it is not possible to calculate the effective electric field. Under these assumptions, the highest technically applied reverse bias of 7V corresponds to an effective reverse bias of -2.5V.

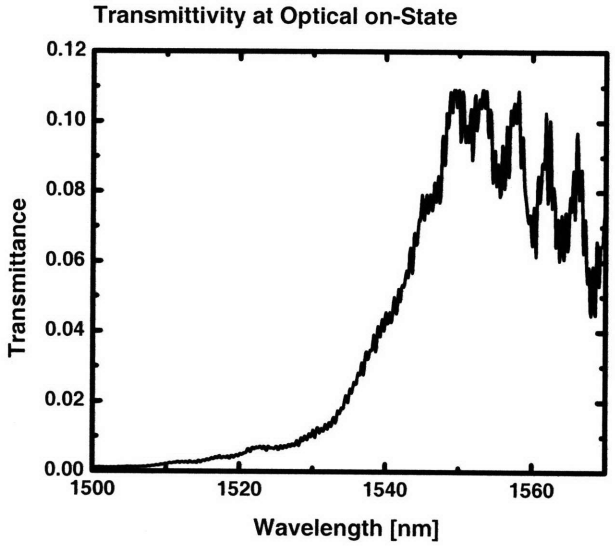

Figure 3.5: Transmittance spectrum of the 50μm electro-absorption Si_xGe_{1-x} modulator at optical "on" state (0V). From the Fabry-Pérot fringes above 1540nm, the absorption loss (2dB) due to indirect band gap absorption is inferred.

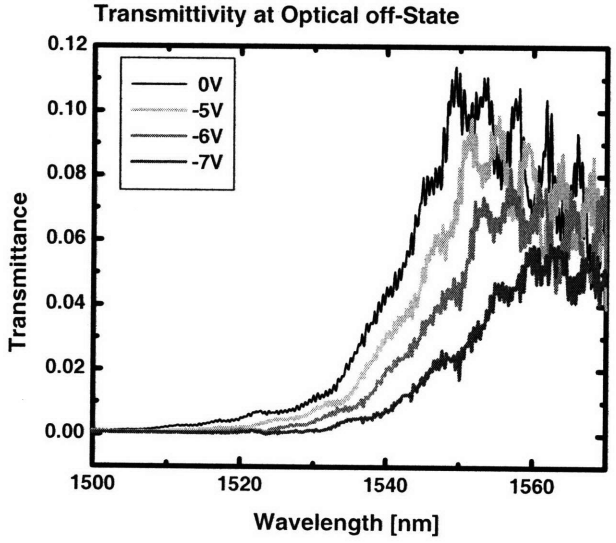

Figure 3.6: Transmittance spectra of the 50μm electro-absorption Si_xGe_{1-x} modulator for three applied voltages: from lighter to darker gray as the applied reverse bias increases (black line at 0V inserted as a reference). Above 1540nm, the slope of direct band gap absorption edge flattens towards longer wavelengths as the applied reverse bias increases.

The achievable modulation depth is wavelength dependent. Figure 3.7 shows 70% modulation depth (5.2dB extinction ratio) in the 1535-1552nm wavelength range, where field-induced direct band edge tilting is observed. High extinction ratio, >7dB (i.e. 80% modulation depth), is obtained in the wavelength range 1510-1533nm with an effective reverse bias of 2.5V (7V). The maximum extinction ratio measured is 14dB (96% modulation depth) at 1523nm; at the wavelength of 1550nm, it measures 6.5dB (78%). The improved performance is due to device design with large overlap between the optical field and the electric field. Modulation depths decreases as lower reverse bias is applied as shown in Figure 3.8(a).

At 1550nm, the maximum modulation depth as a function of reverse effective bias discloses a pseudo-linear behavior with a slope coefficient of 40%/V (achieved modulation depth per applied volt) in the range 0.4V< $V_{effective}$ <2.5V, Figure 3.8(b). Equivalently, in terms of extinction ratio, the slope is 2.2dB/V in the extinction ratio range 0-5.5dB. The ratio between the extinction ratio and the effective applied bias, the effective modulation, could be considered as a new figure of merit of the device. Also shown is the theoretical calculation obtained by inverting the mathematical relationship between the modulation depth and the absorption coefficient which is a function of the applied bias. The theoretical calculation does not predict a linear trend:

$$ModulationDepth = 1 - e^{-\Delta\alpha(V)\cdot L}.$$

Further investigation is needed to understand the experimental behavior. Linear behavior is sought as it would mimic the linear behavior of Mach-

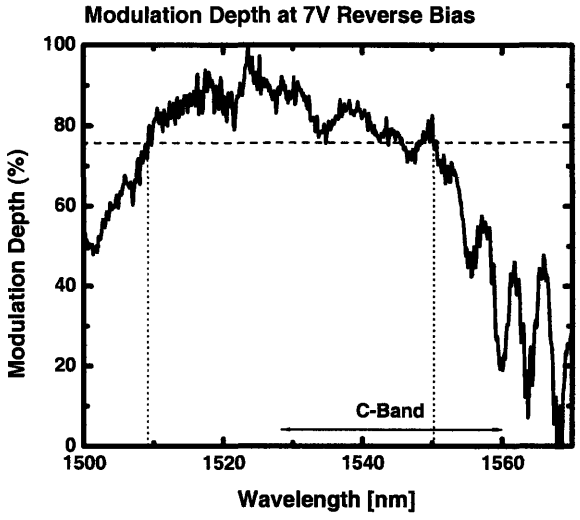

Figure 3.7: Modulation depth of the 50μm electro-absorption Si_xGe_{1-x} modulator when 7V reverse bias is applied. Modulation higher than 78% (6.5dB) can be achieved for a broad wavelength range as indicated in the figure.

Zehnder devices. This feature would allow the device to become marketable in analog applications.

Another fundamental parameter of this modulator is the power consumption per bit of information processed and it can be calculated as $\frac{1}{2}c{\cdot}V^2$, where c is the device capacitance (11fF) and V is the applied effective reverse bias. For example, at 1500nm, with an effective bias of -2.5V, it is as low as 34fJ/bit. Hence, by reducing the capacitance, the driving voltage decreases, as also the energy required per bit.

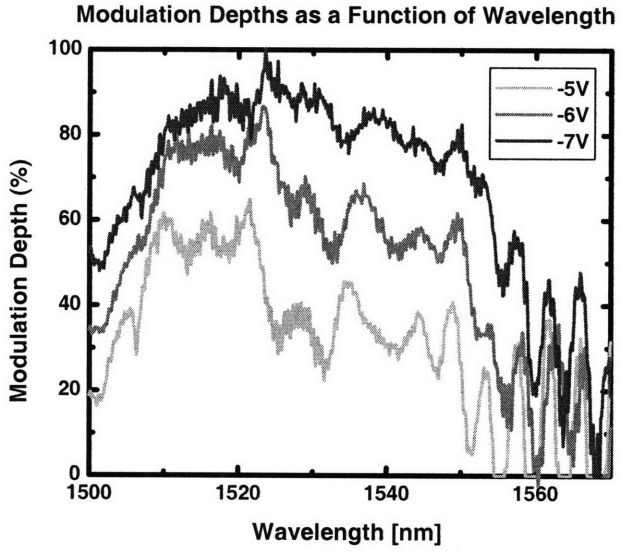

(a)

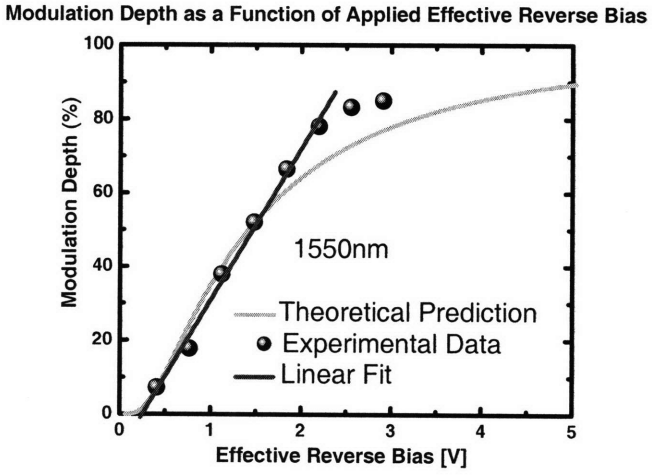

(b)

Figure 3.8: Performance of the 50μm electro-absorption Si_xGe_{1-x} modulator: (a) as-measured modulation performance as a function of wavelength. (b) maximum modulation depth as a function of applied effective reverse bias. Data in (b) is extrapolated from (a). At 1550nm, a pseudo-linear relation is seen between the modulation depth and the applied bias in the range 0.5-2V.

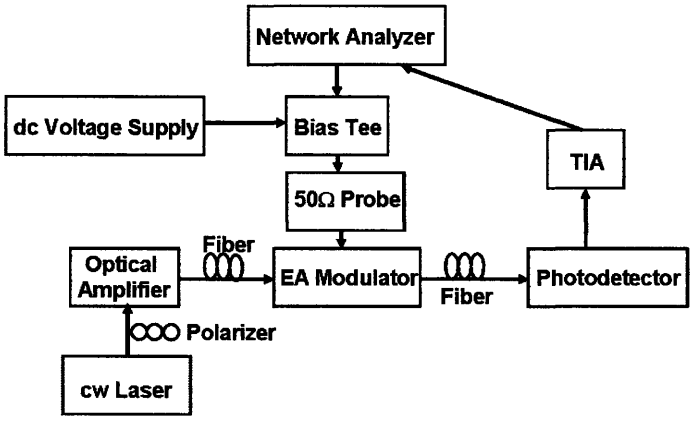

Figure 3.9: Schematic experimental set-up for high frequency measurements.

3.3 High Frequency Measurements

Measurements are performed with a set-up that is schematically drawn in Figure 3.9. A Newport cw laser (1470-1570nm) generates the optical input. Light propagates through a fiber which passes through a polarizer and then through an optical amplifier. The input light is coupled to the on-chip waveguide from the fiber. The dc voltage supply is connected to the device through a bias tee. The RF signal is generated by an Agilent network analyzer and it is delivered to the device through the same bias tee. From the through waveguide, the transmitted light is collected into a fiber which terminates into a photodetector. The photodetector is connected to a transimpedance amplifier which in turn is connected to the network analyzer. As the device has a high series resistance, a 50Ω terminated probe is used to contact the sample to overcome the impedance mismatch.

This system is used to evaluate the dynamic response of the Si_xGe_{1-x} electro-absorption modulator in the high frequencies 10MHz-10GHz range.

The absolute RF power (as measured by the network analyzer) can be

evaluated either as a function of optical input power or as a function of applied reverse bias. Figure 3.10(a) shows the frequency response as a function of the optical input power ranging from 5mW to 25mW while the applied reverse bias is kept constant at a value of -3V. Figure 3.10(b) shows the absolute RF power measured as a function of applied reverse bias (0-5V) while keeping the optical input power constant at 20mW. The 3dB frequency at 3V reverse bias is 1.2GHz. The relatively low 3dB frequency is due to excess series resistance from the electrical contact fabrication processes. In principle the device should have a much higher bandwidth on the order of 100GHz.

It can be seen from Figure 3.10(a) and 3.10(b) that at low frequencies an increased optical input power as well as an increased applied reverse bias increases the detected output power. With the set-up as explained, parasitic inductance could account for the abnormal low-frequency performance. Also, further investigations are necessary to determine whether the high series resistance is frequency dependent and/or applied bias dependent.

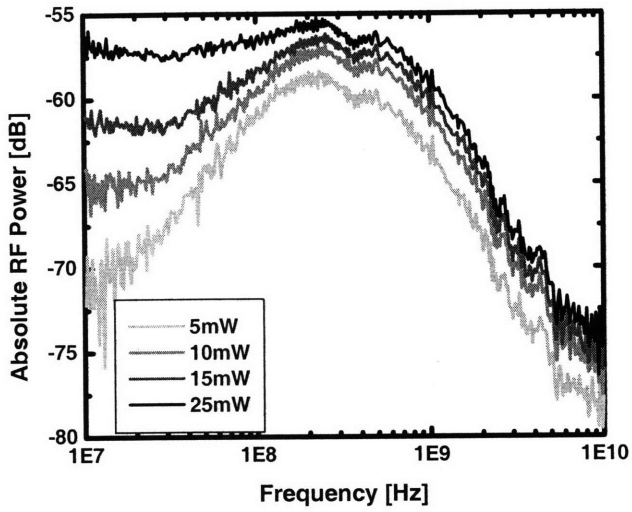

(a)

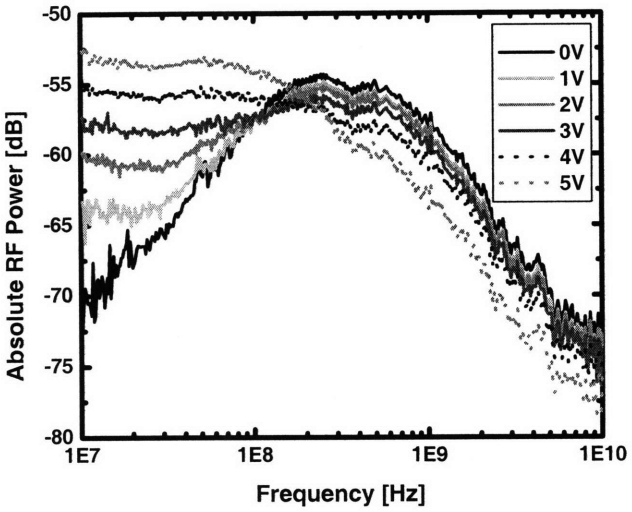

(b)

Figure 3.10: High frequency response of the 50μm electro-absorption Si_xGe_{1-x} modulator. (a) Frequency response at 3V reverse bias as a function of optical input power. (b) Frequency response as a function of applied reverse bias with 20mW fixed optical input.

3.4 Summary

A 50μm long Si_xGe_{1-x} electro-absorption modulator butt-coupled to high index contrast Si/SiO_2 waveguides is experimentally probed. Both low frequency and high frequency measurements are presented. Fabrication over-etching issues, occurred during metal contact deposition, generate a 15kΩ series resistance. The calculated 3dB frequency of this device is of the order of ~100GHz; because of the high series resistance, the expected bandwidth is of 1-1.5GHz. From high frequency measurements, 1.2GHz 3dB bandwidth is determined with an applied reverse bias of 3V. It is experimentally demonstrated that modulation is a result of the electro-absorption effect rather than thermal effects: the slope of the direct band edge tilts towards longer wavelengths as the applied reverse bias increases. 70% modulation depth with low effective driving voltage, -2.5$V_{effective}$, is obtained in the wavelength range 1510-1555nm; while modulation depth higher than 80% is measured in the range 1510-1535nm. At 1550nm, the modulation depth is 78%. The pseudo-linear behavior between the achieved modulation depth and the applied effective voltage suggests that the modulation efficiency, given by the ratio between the extinction ratio and the effective applied bias, could become a new figure of merit of the device. In this case, the modulation efficiency is 2.2dB/V in the extinction ratio range of 0-5.5dB, or equivalently, 40%/V in the effective applied voltage range between 0.4V and 2V. Finally, the power consumption is as low as 34fJ/bit.

Chapter 4

Conclusions and Future Work

Modulators are fundamental building blocks that will enable electronic- photonic integration. The aim of this thesis is to experimentally prove the performance of a novel Si_xGe_{1-x} electro-absorption modulator design, waveguide integrated, butt-coupled to Si/SiO_2 high-index contrast waveguides. Design, fabrication, and experimental results are presented.

As reviewed in the first chapter, the electronic-photonic integration depends on the ability of modulators to fulfill requirements regarding their footprint, driving voltage, modulation depth and speed, as well as insertion loss and temperature insensitive performance. A summary of published Silicon based modulators optimized for applications at 1550nm is given; attention is focused on the evaluation of combinations of optical and electrical structures. Ring modulators have small footprint but they are highly temperature sensitive and they are not broad band devices. In most cases, due to fabrication tolerance, trimming and/or thermal tuning is required to achieve performance at a predetermined wavelength. Mach-Zehnder devices have

larger wavelength range of operation; they are tolerant to small temperature differences but they have large footprint. Published results on Fabry-Pérot based modulators always exploit the use of photonic cavities which are highly sensitive to fabrication and temperature variations.

The second chapter describes the device background both theoretically and with simulations: from the physical modulation mechanism, to the choice of the material, as well as device dimension calculations. The fabrication process flow is also mentioned. The chapter starts with the physical principle on which the modulator is based, the Franz-Keldysh effect. Once the theoretical principle is defined, the best material choice is evaluated and hence the SiGe alloy composition is calculated in terms of the optimization of the device figure of merit. An alloy composition with 0.75% Silicon and with 0.2% tensile strain is determined. For a modulator 50μm long, simulations predict 100GHz 3dB frequency, with 10dB extinction ratio and insertion losses smaller than 5dB.

The experimental device performance is evaluated in the third chapter. IV characterization reveals a high series resistance of the order of 15kΩ that theoretically limits the 3dB frequency to only 1-1.5GHz. dc measurements prove the modulation is a result of electro-absorption effects rather than thermal effects as the slope of the direct band gap tilts towards longer wavelengths with increasing applied reverse bias. 70% modulation depth with low effective driving voltage, -2.5$V_{effective}$, is obtained in the wavelength range 1510-1555nm; while modulation depth higher than 80% is measured in the range 1510-1535nm. At 1550nm, the modulation depth is 78%. Pseudo-

linear behavior between achieved modulation depth and applied effective voltage suggests that the modulation efficiency, given by the ratio between the extinction ratio and the effective applied bias, could become a new figure of merit of the device. Pseudo-linear behavior with a slope of 2.2dB/V is found in the extinction ratio range of 0-5.5dB, or equivalently, a slope of 40%/V in the effective applied voltage range between 0.4V and 2V. From high frequency measurements the 1.2GHz 3dB bandwidth is determined with an applied reverse bias of 3V. Abnormal low-frequency behavior is shown; further investigations are required to explain these results.

The only SiGe modulators as of now published in the literature are by Jonghthammanurak at MIT, [43], and by the Miller's group at Stanford, [44]-[46] . The first one is a Mach-Zehnder device, while the second one is a multi-quantum well device embedded in a Fabry-Pérot cavity. The former one has large footprint, the latter one one works at wavelengths in the range 1440-1460nm and will not be able to reach 1550nm.

Concluding, the SiGe waveguide-integrated modulator optimized for performance at 1550nm described in this thesis represents a breakthrough in modulator research: it has small footprint ($30\mu m^2$), driving effective voltage lower than $2.5V_{effective}$, large modulation depth (>70%) in a broad wavelength range (1510-1555nm), power consumption as low as 34fJ/bit, and 1.2GHz 3dB bandwidth.

4.1 Future work

Suggestions regarding future work can be divided in two distinct phases: the first one refers to the available working devices; the second one would require further fabrication runs.

4.1.1 Current Devices

As mentioned while explaining experimental results, high series resistance is the major issue degrading both electrical and optical performances. Yield is clearly a significant limitation: devices that show open circuit behavior are by far the majority with respect to devices showing diode behavior (one diode-like device out of 1776 in the case of the first probed wafer). This is primarily due to metal contact fabrication-related issues that cause a high series resistance, tens of kΩ while normal contact resistance should be of the order of 10-100Ω. Optical performance is degraded as the expected 3dB frequency (>100GHz) is impossible to reach (the maximum 3dB frequency measured is 1.2GHz at -3V applied bias).

High frequency measurements show abnormal behavior at low frequencies: it is of interest to investigate whether this behavior is due to the high series resistance, to impedance mismatch in the measurement set-up used, to resonances in the system, or to a combination of these factors. Also, it is unknown whether the series resistance is either applied voltage dependent or optical input power dependent, or even frequency dependent. Devices with different series resistance values could be used to exclude or clarify these

possibilities.

Linearity is obstinately sought to mimic Mach-Zehnder devices in order to be useful in analog applications. Unfortunately, for the device being considered, the theoretical equation describing the relation between the maximum modulation depth (measured at a specific wavelength) and the applied reverse bias is not linear. The pseudo-linear relation that is found (40%/V in the range 0.5V< $V_{effective}$ <2.5V) is only an experimental observation which should be confirmed by expanding the measurements to all devices that are in dies showing similar electrical diode-like behavior. Simulations of similar devices could also reveal if it is possible to create a device that transforms the relation between the modulation depth achieved and the applied reverse bias to a truly linear relation, where "truly linear" implies linearity in both theory and experimental observations.

4.1.2 Fabrication Implementation

The measured 3dB bandwidth of the 50μm Si_xGe_{1-x} electro-absorption modulator is 1.2GHz. Theoretical calculations predicted this value to be higher than 100GHz as the only limitation should be RC with an extinction ratio higher than 10dB. These values are not reached due to major fabrication issues during metal contact fabrication. The origin of the over-etching beneath the metal contacts causing high series resistance should be understood and avoided.

Also, metal fill used for chemical-mechanical polishing drastically deteriorates optical propagation in waveguides. Waveguide loss is estimated to be as

high as 30dB/cm thanks to the metal layer being too close to the waveguide layer. This layer should be either etched after the polishing is performed, or it should be placed further away from the waveguide layer. Most of the electrically active devices would then also be optically transparent.

These improvements would increase yield, and would allow measuring devices with $\sim$100GHZ 3dB frequency, extinction ratio >10dB, low driving voltage and small footprint.

Bibliography

[1] Peercy PS, "The Drive to Miniaturization", Nature **406**, 1023-1026 (2000)

[2] Parry G, "Silicon's New Shine", Nature **437**, 1244 (2005)

[3] Lipson M, "Overcoming the Limitations of Microelectronics Using Si Nanophotonics: Solving the Coupling, Modulation and Switching Challenges", Nanotechnology **15**, S622-S627 (2004)

[4] Lipson M, "Guiding, Modulating, and Emitting Light on Silicon - Challenges and Opportunities", Journal of Ligthwave Technology **23**, 4222-4238 (2005)

[5] Manolatou C and Lipson M, "All-Optical Modulators Based on carrier Injection by Two-Photon Absorption", Journal of Lightwave Technology **24**, 1433-1439 (2006)

[6] Almeida VR, Barrios CA, Panepucci R, and Lipson M, "All-Optical Control of Light on a Silicon Chip", Nature **431**, 1081-1084 (2004)

[7] Lipson M, "Switching Light on a Silicon Chip", Optical Materials **27**, 731-739 (2005)

[8] Xu Q, Almeida VR, and Lipson M, "Micrometre-Scale All-Optical Wavelength Conveter on Silicon", Optics Express **14**, 9430-9435 (2006)

[9] Almeida VR and Lipson M, "Optical Bistability on a Silicon Chip", Optics Letters **29**, 2387-2389 (2004)

[10] Xu Q and Lipson M, "Carrier-Induced Optical Bistability in Silicon Ring Resonators", Optics Letters **31**, 341-343 (2006)

[11] Lipson M, "Compact Electro-Optic Modulators on a Silicon Chip", IEEE Journal of Selected Topics in Quantum Electronics **12**, 1520-1526 (2006)

[12] Xu Q, Schmidt B, Pradhan S, and Lipson M, "Micrometre-Scale Silicon Electro-Optic Modulator, Nature **435**, 325-327 (2005)

[13] Preble SF, Xu Q, Schmidt BS, and Lipson M, "Ultra-Fast all-Optical Modulation on a Silicon Chip", Optics Letters **30**, 2891-2893 (2005)

[14] Xu Q, Schmidt B, Shakya J, and Lipson M, "Cascaded Silicon Micro-Ring Modulators for WDM Optical Interconnection", Optics Express **14**, 9431-9435 (2006)

[15] Xu Q, Manipatruni S, Schmidt B, Shakya J, and Lipson M, "12.5Gbit/s Carrier-Injection-Based Silicon Micro-Ring Silicon Modulators", Optics Express **15**, 430-436 (2007)

[16] Manipatruni S, Xu Q, and Lipson M, "PINIP Based High-Speed High-Extinction Ratio Micron-Size Silicon Electro-Optic Modulator", Optics Express **15**, 13035-13042 (2007)

[17] Barrios CA and Lipson M, "Modeling and Analysis of High-Speed Electro-Optic Modulation in High Confinement Silicon Waveguides Using Metal-Oxide-Semiconductor Configuration", Journal of Applied Physics **96**, 6008-6015 (2004)

[18] Lipson M, "Switching light on a silicon chip", Optical Materials **27**, 731-739 (2005)

[19] Almeida VR, Xu Q, and Lipson M, "Ultrafast Integrated Semiconductor Optical Modulator Based on the Plasma-Disperion Effect", Optics Letters **30**, 2403-2405 (2005)

[20] Liu A, Liao L, Rubin D, Nguyen H, Ciftcioglu B, Chetrit Y, Cohen R, Izhaky N, Basak J, and Paniccia M, "Recent Advances in High Speed Silicon Optical Modulator", Proceedings of SPIE **6477**, 647710 (2007)

[21] Liu A, Liao L, Rubin D, Nguyen H, Ciftcioglu B, Chetrit Y, Izhaky N, and Mario Paniccia , "High-speed optical modulation based on carrier depletion in a silicon waveguide", Optics Express **15**, 660-668 (2007)

[22] Green WMJ, Rooks MJ, Sekaric L, Vlasov YA, "Ultra-Compact, Low RF Power, 10Gb/s Silicon Mach-Zehnder Modulator", Optics Express**15**, 17106-17113 (2007)

[23] Liu A, Jones R, Liao L, Samara-Rubio D, Rubin D, Cohen O, Nicolaescu R, and Paniccia M, "A High-Speed Silicon Optical Modulator Based on a Metal-Oxide-Semiconductor Capacitor", Nature **427**, 615-618 (2004)

[24] Liu A and Paniccia M, "Advances in Silicon Photonic Devices for Silicon-Based Optoelectronic Applications", Physica E **35**, 223-228 (2006)

[25] Izharky N, Morse MT, Koehl S, Cohen O, Rubin D, Barkani A, Sarid G, Cohen R, and Paniccia M, "Development of CMOS-Compatible Integrated Silicon Photonics Devices", IEEE Journal of Selected Topics in Quantum Electronics **12**, 1688-1698 (2006)

[26] Liao L, Samara-Rubio D, Morse MT, Liu A, Hodge D, Rubin D, Keil UD, and Franck T, "High Speed Silicon Mach-Zehnder Modulator", Optics Express **13**, 3129-3135 (2005)

[27] Liao L, Samara-Rubio D, Liu A, Rubin D, Keil UD, Franck T, Hodge D, and Paniccia M, "High Speed Metal-Oxide-Semiconductor Capacitor-Based Silicon Optical Modulators", Japanese Journal of Applied Physics **45**, 6603-6608 (2006)

[28] Lipson M and Kimerling LC, "All Optical Switch for Optical Integrated Circuits", United States Patent, Patent No.: US 6,684,003 B2 (2004)

[29] Barrios CA, Almeida VR, and Lipson M, "Low-Power-Consumption Short-Lenght and High-Modulation-Depth Silicon Electro-Optic Modulator", Journal of Lightwave Technology **21**, 1089-1098 (2003)

[30] Barrios CA, Almeida VR, Panepucci R, and Lipson M, "Electrooptic Modulation of Silicon-on-Insulator Submicrometer-Size Waveguide Devices", Journal of Lightwave Technology **21**, 2332-2339 (2003)

[31] Schmidt B, Xu Q, Shakya J, Manipatruni S, and Lipson M, "Compact Electro-Optic Modulator on SIlicon-on-Insulator Substrates Using Cavities with Ultra-Small Modal Volume", Optics Express **15**, 3140-3148 (2007)

[32] Liu J, Sun X, Pan D, Wang X, Kimerling LC, Koch TL, and Michel J, "Tensile-Strained, n-Type Ge as a Gain Medium for Monolithic Laser Integration on Si", Optics Express **15**, 11272-11277 (2007)

[33] Shen H and Pollak FH, "Generalized Franz-Keldysh Theory of Electromodulation", Physics Review B **42**, 7097-7102 (1990)

[34] Frova A, Handler P, Germano FA, and Aspnes DE, "Electro-Absorption Effects at the Band Edges of Silicon and Germanium", Physics Review **145**, 575-583 (1966)

[35] Chuang SL, "Physics of Optoelectronic Devices", Wiley Series in Pure and Applied Optics, Chapter 13, Goodman JW Series Editor (1995)

[36] Liu J, "GeSi Photodetectors and Electro-absorption Modulators for Si Electronic-photonic Integrated Circuits", PhD Thesis, MIT (2007)

[37] Pollak FH and Cardona M, "Piezo-Electroreflectance in Ge, GaAs, and Si", Physics Review **172**, 816 (1968)

[38] Pickering C, Carline RT, Robbins DJ, Leong WY, Barnett SJ, Pitt AD, and Cullis AG, Journal of Applied Physics **73**, 239 (1993)

[39] Weber J and Alonso MI, "Near-band-gap photoluminescence of Si-Ge alloys", Physics Review B **40**, 5683(1989)

[40] Madelung O, Landolt-Börnstein, Properties of Group IV elements and III-V, II-VI, and I-VII Compounds, Numerical Data and functional relationships in science and technology Vol 17a, chapter 1.6, Springer (Berlin) 1982

[41] Humlicek J, Properties of strained and relaxed Silicon and Germanium, EMIS Datareviews Series, No 12, INSPEC, London (1995), chapter 4.

[42] Madelung O, Landolt-Börnstein, Properties of Group IV elements and III-V, II-VI, and I-VII Compounds, Numerical Data and functional relationships in science and technology Vol 17a, chapter 1.6, Springer (Berlin) 1982

[43] Jonghthammanurak S, "Ge-rich SiGe Materials for Field-Effect Modulator Applications", PhD Thesis, MIT (2008)

[44] Kuo YH, Lee YK, Ren Y, Roth JE, Kamins TI, Miller DAB, and Harris JS, "Strong Quantum-Confined Stark Effect in germanium Quantum-Well Structures on Siliocn", Nature **437**, 1334-1336 (2004)

[45] Roth JE, Fidaner O, Schaevitz RK, Kuo YH, Kamins TI, Harris JS, and Miller DAB, "Optical Modulator on Silicon Employing Germanium Quantum Wells", Optics Express **15**, 5851-5859 (2007)

[46] Okyay AK, Pethe AJ, Kuzum D, Latif S, Miller DAB, and Saraswat KC, "SiGe Optoelectronic Metal-Oxide Semiconductor Field-Effect Transistor", Optics Letters **32**, 2022-2024 (2007)